# REDUCED DENSITY HYDROGENATED SILICON THROUGH REACTIVE DC MAGNETRON SPUTTERING WITH SECONDARY RF PLASMA DISCHARGE FOR EUV MULTILAYER MIRROR APPLICATION

BY

JAN PETER UHLIG

THESIS

Submitted in partial fulfillment of the requirements
for the degree of Master of Science in Nuclear, Plasma, and Radiological Engineering
in the Graduate College of the
University of Illinois at Urbana-Champaign, 2019

Urbana, Illinois

Master's Committee:

Professor David N. Ruzic, Advisor
Research Assistant Professor Daniel Andruczyk

## Abstract

In Extreme Ultra-violet Lithography applications Si/Mo Multi-Layer Mirrors are used to collect, transmit and focus EUV light. While current MLMs have reached the practical limit achievable with current materials, the per mirror efficiency is still suboptimal, especially in a projection lithography system with a multitude of these mirrors. A method of improvement then, without significantly modifying the mirror itself or the process for manufacture of the mirrors, is to replace the Si spacer layer found in EUV mirrors, with a reduced density Si layer. Theory predicts that such a modification, if done without introducing contaminants that absorb EUV themselves, can marginally increase the per mirror efficiency. When this per mirror marginal improvement is then applied to all mirrors in a lithography system the end result comes out to be a two-fold or more increase in efficiency of the system.

Investigated in this work then is a method for replacing the Si film with a reduced density Si:H film, through the modification of the standard DCMS deposition process through reactive DCMS with hydrogen, along with a secondary RF plasma to aide in radical generation. The eventual goal is to produce both hydrogenated and non-hydrogenated MLMs to the same specifications, which can then be tested for EUV reflectivity, proving the initial theory.

In the process for producing the low density hydrogenated Si film discussed the main issue that presented itself was the formation of $H_2$ gas blisters in the film, likely at subsurface interfaces, leading to structures that project beyond the surface of the film. Methods for the avoidance of these blisters are discussed and applied, leading, among others, to Si:H films with a density of 1.73 g/cm$^3$, with lesser numbers and smaller blisters than previously observed. Finally, successful attempts are also made at producing multilayers at the appropriate size for EUV reflectivity, that is with a bilayer thickness of 6.9 nm.

## Acknowledgements

I would like to thank a number of people, who have assisted me in producing this thesis work, which would certainly not have been possible without them.

First, I would like to thank my advisor, Prof. Dr. David N. Ruzic, for his guidance both during the experimental and writing phases, as well as for coming up with the underlying concept which lead to this research.

Next, I would like to thank Dr. Eitan Barlaz, and Dr. Ivan Shchelkanov, who both assisted me greatly as Post-Docs in our lab. Both provided significant insight and assistance both in trouble shooting, ideas, and data interpretation.

Additionally, I would like to thank Nathan Bartlett, who, as my sole undergraduate assistant, assisted me greatly in getting the experiment into operating shape, as well as establishing initial operational procedures.

Looking outside of my laboratory, first off, this research was carried out in part in the Frederick Seitz Materials Research Laboratory Central Research Facilities, University of Illinois. There, I would particularly like to thank Dr. Mauro Sardela for his assistance with the PANalytical X-ray diffractometer, and persuading the device to take the particular data that was desired.

# Table of Contents

*1. Introduction* ____ *1*

*2. Theory* ____ *5*

**2.1 Why Hydrogenated, Amorphous Silicon?** ____ **5**

**2.2 Direct-Current Magnetron Sputtering** ____ **9**

**2.3 RF Plasmas and Matching Network** ____ **12**

**2.4 XRR Theory** ____ **13**

**2.5 Radical Probe Theory** ____ **14**

*3. Setup/Methodology* ____ *17*

**3.1 Experimental Setup (SHADE)** ____ **17**

3.1.1 Vacuum Chamber SHADE ____ 17

3.1.2 LabVIEW Control Program ____ 22

**3.2 XRR Data Collection and Modelling** ____ **24**

3.2.1 XRR Data Collection ____ 24

3.2.2. What is IMD? ____ 25

3.2.3 Conversion of Data formats ____ 25

3.2.4 Single Layer Modelling ____ 26

3.2.5 Multilayer Modelling ____ 30

**3.3 Radical Probe Manufacture and Installation** ____ **31**

**3.4 AFM** ____ **32**

*4. Results and Discussion* ____ *33*

**4.1 Mo Films** 33

**4.2 Si Films** 36

**4.3 Si:H Films** 39

4.3.1 Radical Probe Results 49

**4.4 Multilayer Films** 52

***5. Conclusion*** 55

***6. Future Work*** 56

***7. References*** 58

# 1. Introduction

Moore's Law is a longstanding defining "rule of thumb" derived from an observation made by Gordon Moore in 1965, stating that the number of transistors in a dense integrated circuit would double approximately every two years. [1] Great effort has been put into maintaining the validity of Moore's Law since those days. One of the primary, limiting factors that needs to be solved in order to adhere to Moore's Law, is the difficulty of generating ever smaller features without significant loss of throughput, i.e. using lithographic techniques. What this, in general terms, means, is the need for smaller wavelength light sources and accompanying equipment, with the next step being extreme ultra-violet light (EUV), corresponding to a wavelength of 13.5 nm.

EUV lithographic technique applications in the modern semiconductor manufacture industry utilize projection lithography setups. In general, each setup of this type requires 10-11 mirrors. Current commercial EUV mirrors are multi-layered mirrors, and are ~69% efficient individually. [2] This results in approximately 2% of the light initially generated to end up being used in the lithographic process. All other light is lost during focusing.

Before the introduction of Multi-Layer Mirrors (MLM), single layer grazing incidence optics were used to reflect X-Ray/Soft X-ray wavelength due to the reflectivity being approximately zero at angles outside a small band around grazing incidence [3]. The advent of multi-layers changed this by introducing a structure which can effectively reflect (soft) X-Rays via constructive interference off of multiple layers. This requirement on the mirror is accounted for through the Bragg condition, leading to a resultant bilayer thickness of 6.9 nm for the EUV wavelength of 13.5 nm.

Materials choices need then be made dependent upon the optical constants of the materials, as well as taking into account the absorption edges of the materials. For EUV applications, MLMs

are typically made from molybdenum and silicon. Molybdenum acts as the high-Z reflective layer, which reflects the soft X-Rays at its boundaries. Si is used as the low-Z or spacing layer. The use of Si in EUV MLMs derives from its low absorption at EUV wavelengths, though it is worth noting that its absorption increases dramatically below a wavelength of 12.4 nm. [3] Typical, commercial MLMs are made up of 40-50 bilayer periods, and produced via Direct Current Magnetron Sputtering (DCMS) deposition upon a pre-formed substrate of appropriate shape.

Even though MLMs provide significant benefits over single layer mirrors, they still contain space for improvement. The primary method for improving the reflectivity of the MLM is through the reduction of the density of the Si spacer film. Simple modelling shows clearly the impact that a reduction in density of the Si film can have upon the reflectivity.

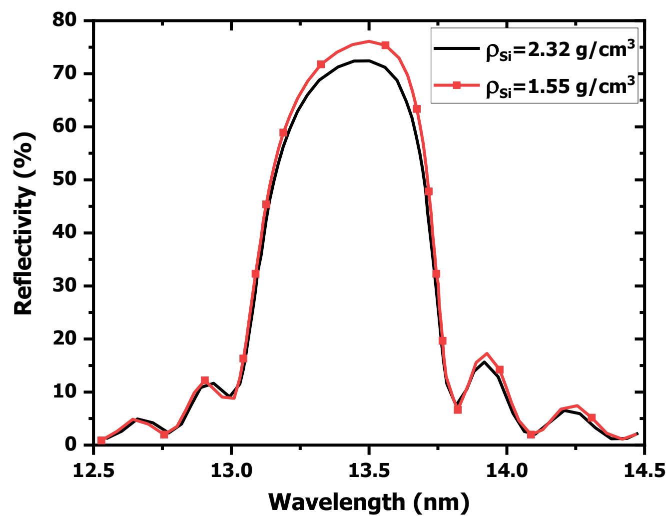


*Figure 1: Simulation of EUV reflectivity of a standard MLM (Black) as compared to a reduced Si density (1.55 g/cm$^3$) MLM (Red). Shows theoretical gain in EUV reflectivity achieved by replacement of the standard density Si spacing layer found in current, commercial EUV mirrors, by a reduced density (in this case 1.55 g/cm$^3$) Si spacing layer. 1.55 g/cm$^3$ was chosen for the purpose of simulation due to being the lowest previously achieved Si:H density in literature. [4] Model created using Kohn's solutions for Fresnel equations [5] in model available on the Lawrence Berkeley National Laboratory website. [6] [7]*

As commercial mirrors are produced via DCMS it then follows that an ideal method of improving the MLMs is through minor modification of the pre-existing DCMS process to produce a reduced density Si film. The preferred method investigated here is through the addition of H radicals in the deposition process, producing a hydrogenated Si film. The use of Hydrogen, as

opposed to Boron, Oxygen, or Carbon is due to significant absorption of EUV light that these elements provide, an effect that can easily outweigh the benefits achieved in reducing the density.

To achieve this reduced density, hydrogenated Si film a number of approaches can be taken. Ion bombardment of either the individual Si layers in the multilayer structure, or of the final multilayer are non-feasible, due to the damage this will cause to the structure. Additionally, the formation of $H_2$ blisters has been observed in MLMs when cleaned with a hydrogen plasma, or exposed to H ion bombardment. [8] [9] Similarly, hydrogen molecules cannot be incorporated due to their mobility in molybdenum. [10]

A source of H radicals is then necessary during the deposition of the Si films. The simplest is the addition of $H_2$ into the operating gas mixture during the deposition of the Si film, relying upon the magnetron plasma to break these molecules into H radicals. While this option is simple, it offers no outside control over the radical density, other than by increasing the $H_2$ partial pressure, preventing any significant tuning of the process. Additionally, as the cracking of the $H_2$ molecules will occur close to the target and H ions will inevitably be generated and accelerated towards the target the drawn current will increase without an increase in sputtering yield, or, alternatively, the sputtering yield will decrease with constant current.

This then leads to the need of providing H radicals from an external source. Something like a dedicated ion source may work, but would likely require differential pumping of the system, as well as being difficult to scale up for a production environment.

The approach taken in this work is provide H radicals through the addition of $H_2$ into the working gas mixture, while generating a secondary plasma closer to the substrate. This can be done easily with an RF plasma source, either inductively coupled (ICP) or capacitively coupled (CCP), either of which is likely to provide sufficient uniformity over a production grade mirror

substrate. Additionally, it has been previously established that a secondary RF ICP plasma does not significantly impact the stability or performance of magnetrons operation. [11]

# 2. Theory

## 2.1 Why Hydrogenated, Amorphous Silicon?

As the entirety of this project depends on the concept of using reduced density, hydrogenated, amorphous Silicon, it is worth discussing in depth why it is desirable for the reader that is not satisfied for the abbreviated explanation given in the introduction. To make sense of it, one has to start with a discussion of the functionality of soft X-ray mirrors. It is also worth noting that this entire section is an abbreviated overview of a significant portion of Kozhevnikov and Vinogradovs 1995 paper titled "Multilayer X-ray Mirrors" [3], and the interested reader is encouraged to refer to it for a more thorough understanding of the specifics. It is also noted that symbols used are changed from the reference text where appropriate to stay consistent within the body of this text.

The first thing of note is that before the advent of multilayer mirrors, single layer grazing incidence mirrors were used for the reflection of soft X-rays, which reflect a significant portion of soft X-rays only at extremely small grazing angles. Alternatively, a properly calibrated multilayer can reflect soft X-rays at angles closer to normal incidence to a significant extent, while being comparable at grazing angles.

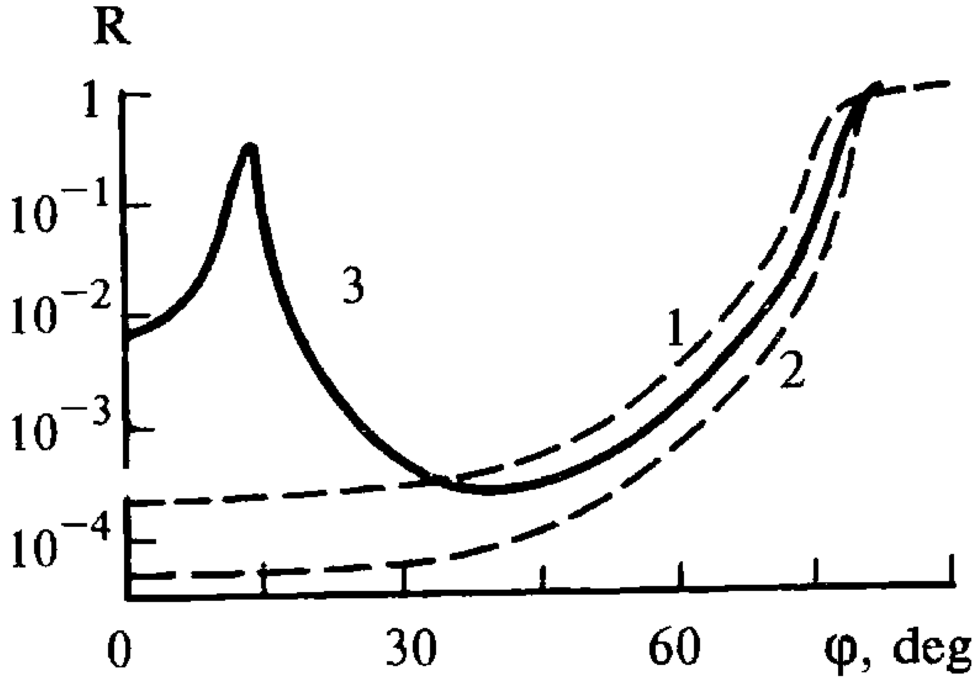


*Figure 2: From Kozhevnikov et al., Shows the angular dependence of the reflectivity of a soft X-ray wavelength of 93.4 A for (1) a molybdenum single layer mirror, (2) a boron single layer mirror, and (3) for the 200 bilayer thick Mo/Bo multilayer (19.1 A and 29.9 A respectively). $\psi$ is the angle of incidence with respect to normal incidence. [3]*

Reflection in multilayer mirrors is based on the structural interference of the waves reflected from various interfaces in the multilayer stack. This means that, inherently, their reflection is dictated by the Bragg condition.

$$2d\ cos\psi \simeq n\lambda,\ n = 1,2,\dots \qquad [1]$$

Where d is the multilayer structure period and $\psi$ is the angle of incidence. The Bragg condition is then the first condition that must be satisfied, which in turn means that the individual waves reflected from each boundary interfere constructively. It can be seen that at close to normal incidence the thickness of the bilayer, d, must then be on the order of Angstrom to nanometer thick.

At this point, the main question left if one were trying to produce a multilayer mirror is that of materials choice, and exact sizes of the two layers that make up the bilayer. It is worth noting here that in the ranges of wavelengths of soft X-rays most materials have large absorption cross

sections, which inherently limits options. In order to actually choose which materials, and, by extension, the structure of the multilayer, one must look in more depth at the optical equations governing the reflectivity.

$$f = \frac{Re(\epsilon_1 - \epsilon_2)}{Im(\epsilon_1 - \epsilon_2)},\ \ g = \frac{Im\,\epsilon_2}{Im(\epsilon_1 - \epsilon_2)},\ \ y = \frac{\pi(\Gamma + g)}{\sin \pi\Gamma},\ \ \xi = \frac{|f\sigma|}{y} \qquad [2]$$

Where $\epsilon_{1,2}$ are the permittivities of the reflective and spacing layer (referred to as the strong ad weak absorber in [3]), $\Gamma = t_1/d$ that is the ratio of the reflective layer thickness to the thickness of the bilayer, and $\sigma$ is either 1 for s polarization of the light, or $\cos 2\psi$ for p polarization.

For maximum reflectivity, the parameter Γ must satisfy the equation

$$\tan \pi\Gamma = \pi(\Gamma + g) \qquad [3]$$

The maximum reflectivity, $R_{max}$, is then

$$R_{max}^{s,p} = \frac{1 - u_{min}^{s,p}}{1 + u_{min}^{s,p}},\quad u_{min}^{s,p} = \left(\frac{1 - \sigma_0^2 \cos^2 \pi\Gamma}{1 + f^2\sigma^2 \cos^2 \pi\Gamma}\right) \qquad [4]$$

The optimal ratio of thicknesses, Γ, then does not depend upon the polarization of the light, or the angle of incidence, but only upon the ratio of the linear absorption factors of the two materials in the multilayer. This relation, in combination with the absorption profiles of the materials in consideration, determine the materials choice to be used for the wavelength being considered. In the case of 13.5 nm wavelength EUV light, this leads to the selection of molybdenum (Mo) for the reflective layer, and silicone (Si) for the spacing layer. This leads to a maximum theoretical reflectivity of 74%. [2] While this is respectable, as has been mentioned before, in a system with 10 or 11 mirrors, this still leads to a paltry fraction of the initial light sources intensity delivered to the target, and as such improvements are desirable.

This in turn leads to the concept of a reduced density spacing layer. By decreasing the density of the spacing layer ($\rho_2$ based on previous convention), one decreases both the absorption in the

entire structure, by virtue of decreasing the density of potential absorbers the light may encounter, as well as decreasing the factor g, which was defined above. Lastly, a decrease in the density of the spacer layer will lead to an increase in the factor |f|, which is indicative of an increase in the interference effects, as well as an increase in the Fresnel reflectivity from the individual bilayer boundaries. All this will lead, together, to an increase in the total reflectivity.

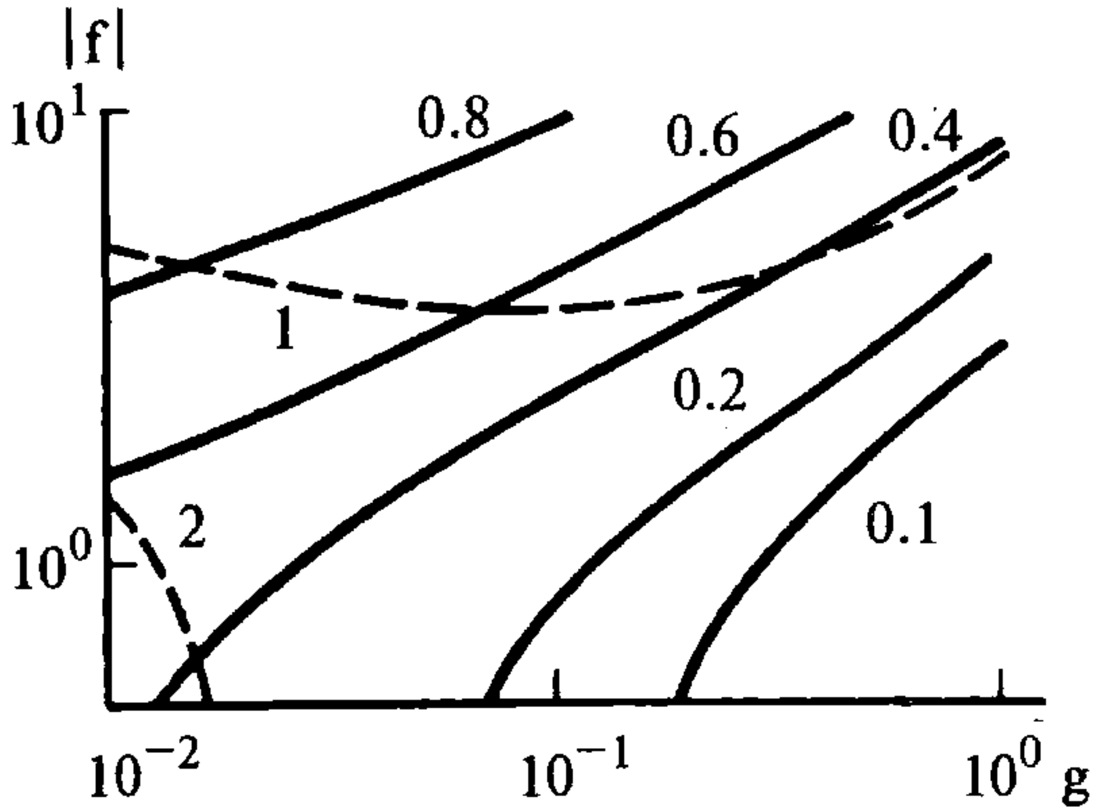


*Figure 3: Reproduced from Kozhevnikov et al. Plot showing $R_{max}$ = constant lines as both g and |f| vary for the case of normal incidence. As can be seen from this, a decrease in g, or an increase in |f| will lead to an increase in $R_{max}$. [3]*

While this provides a reasonable understanding as to why a decreased density spacer film is desirable, it does not sufficiently answer the question as to why a hydrogenated, reduced density Si film is a good solution. For example, while a reduced density Si film of 1.55 g/cm$^3$ has been shown [4], materials such as SiOC:H have been reported with densities as low as 1.2 g/cm$^3$ [12]. Similarly, incorporation of boron into the Si film is not feasible as boron absorbs at the 13.5 nm

wavelength. [13] [14] The reason for the selection of reduced density Si:H films then is due to the aforementioned high absorption of most materials in the soft X-ray/EUV spectrum. As can be seen below in Figure 4, while in the case of replacing the Si spacer layer with a reduced density Si:H layer (at 1.55 g/cm$^3$) yields an increase in the reflectivity in the main peak, if instead the Si spacer layer is replaced with a SiOC:H layer with a density of 1.2 g/cm$^3$, then not only is a significant portion of EUV reflectivity lost due to absorption by the oxygen and carbon, the main peaks also shifts due to this change in chemistry.

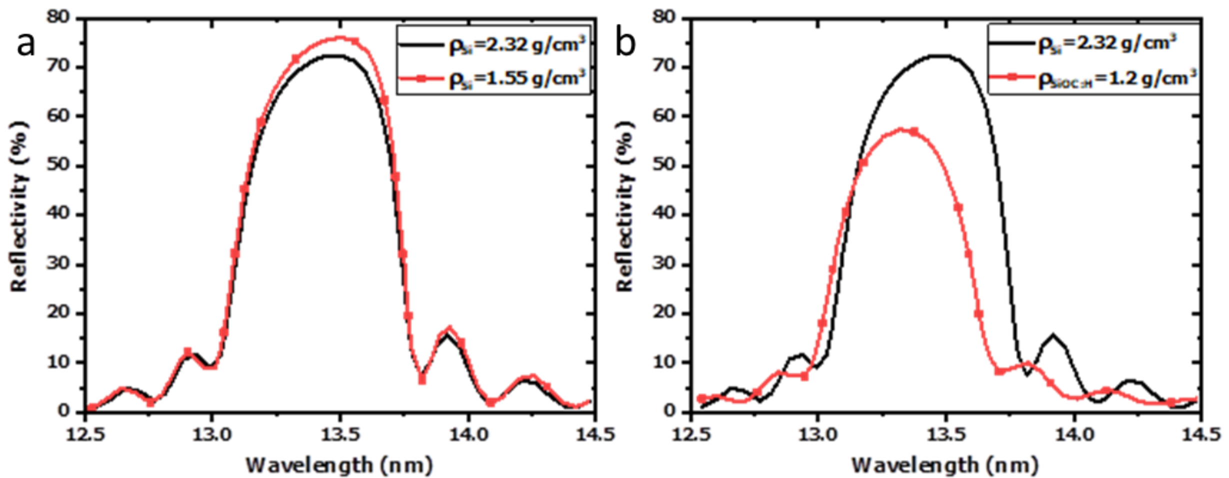


*Figure 4: a) repeat image showing the comparative EUV reflectivity of a normal Si/Mo Multilayer plotted against a reduced density Si:H/Mo multilayer with a Si:H density of 1.55 g/cm$^3$. b) Comparative EUV reflectivity of a standard Si/Mo multilayer with a SiOC:H/Mo multilayer with a SiOC:H density of 1.2 g/cm$^3$. Clearly shows the losses in EUV reflectivity incurred by the inclusion of oxygen and carbon in the spacer layer, and that this loss far outweighs any potential gains from the significantly reduced density in this case.*

## 2.2 Direct-Current Magnetron Sputtering

Direct-Current Magnetron Sputtering, or DCMS for short, is physical vapor deposition (PVD) technique which relies on a steady ion bombardment for sputtering of the material of interest due to an electron current which is trapped in an ExB drift in the immediate super-surface region. The magnetic flux is provided by a built-in set of permanent magnets, with an electric field generated between the biased target and surrounding ground. It is worth establishing here that the term

“target” is used here to refer to the top most plate of material that is to be sputtered and is, as such, an interchangeable component to be consumed.

In operation, a DC magnetron has an applied bias which, initially, strikes a plasma which is subsequently maintained. The electrons are trapped due to the ExB drift, continually ionizing neutral gas particles that exist in the area of confinement. This continuously produces ions and electrons, offsetting losses to lack of confinement or recombination. The bias applied to the magnetron is always negative, and acts to accelerate the ions produced in this electron confinement region, commonly referred to as the race track as the electrons “race” around it, towards the target. On impact, the ions can knock an atom from the surface, sputtering it. Sputtered material leaves the magnetron eventually depositing somewhere in the vacuum chamber, ideally upon the substrate to be covered. The distribution of the sputtered material is dependent upon the configuration of the underlying magnets.

The rate of deposition upon the substrate is dependent upon the solid angle subtended by the sample, the operating pressure, and the sputtering rate. The solid angle affects the quantity of sputtered material that is, under non-collisional conditions, expected to hit the area of the sample. The pressure has a standalone effect pertaining to mean free path of the sputtered material, and the probability of collisions scattering the sputtered material thereby spreading the sputtered material beyond the roughly half-sphere region of deposition that the directionality of a magnetron sputtering discharge implies.

Lastly, most importantly, and most modifiable the sputtering rate is directly related to the deposition rate: the more material that is sputtered per unit time, the more has to deposit itself per unit time across the entire area deposited. The sputtering rate is a function of two variable: the sputtering yield per incident particle (generally per incident ion), and the rate at which these

particles are incident upon the target. The sputtering yield is dependent primarily upon the energy of the incident particle: below a threshold, an insignificant amount of energy is imparted into the surface and immediate subsurface target particles, insufficient to break them out of their bonded state and sputter them. Within a range, typically ~200-1000V (for $Ar^+$ ions) a sufficient quantity of energy is deposited close to the surface to sputter material, with the exact yield dependent upon the exact energy (or, approximately, the voltage applied to the target). A secondary variable that affects the sputtering yield is the ratio of masses between the incident ion and the material to be sputtered. Masses too greatly different form one another are likely to prevent significant energy transfer during collision, preventing sputtering. A tertiary effect that affects the deposition rate is the angle of incidence of the ion: at angles close to normal incidence the ion will penetrate more deeply into the target, therefore depositing its energy further away from the surface, thereby sputtering less. Maximum sputtering occurs at an intermediate angle, where the chance of deflection of the ion is not yet significant, but the angle is great enough to ensure most of the deposited energy is deposited close to the surface. As alluded to, at angles too close to grazing incidence the incident ion is generally deflected, without depositing much energy, thereby preventing significant sputtering. [15] Addressing the matter of quantity of incident ions per unit time, this is essentially equivalent to the current drawn by the magnetron. While part of this current will inevitably be made up of particles arriving at the target with lower energy, potentially even below the sputtering threshold, the quantity of ions with energy sufficient to sputter material is directly related to the total current and, as such, for control of the magnetron the current drawn can be used as a direct control over the sputtering yield, as long as the voltage remains relatively unchanged.

Reactive Sputtering is a slight modification of standard magnetrons puttering, be it DC, RF, or HiPIMS (High Power Impulse Magnetrons Sputtering), and is, at a basic level, achieved via the introduction of a reactive gas species into the operating gas mixture.

## 2.3 RF Plasmas and Matching Network

Inductively Coupled Plasmas (ICPs), a subset of Radio Frequency (RF) Plasmas, provide a convenient and simple way of generating a plasma in a low pressure system. In an ICP system, the electrode, here a coil, is biased using a high voltage, RF bias at 13.56 MHz. This bias generates a large sheath drop which initially accelerates electrons, breaking down the gas in the system if the overall pressure is sufficiently low, generally sub 100's mTorr pressures. [16] The RF currents running through the RF coil generates a time-varying RF magnetic flux density in the surrounding area, which in turn induces a time varying electric field according to Faraday's Law. This "inductive" electric field then actually accelerates the electrons, sustaining the plasma discharge. [17]

In order to maximize the RF current driven through the antenna, a resonant circuit is required, generally referred to as a matching network. While differing setups exist, the standard which is used here is an L-type matching network, which consists of, from the output of the RF power supply, a variable "tuning" capacitor and variable inductor in line with the RF coil, and a variable "load" capacitor to ground in parallel with the rest. [18]

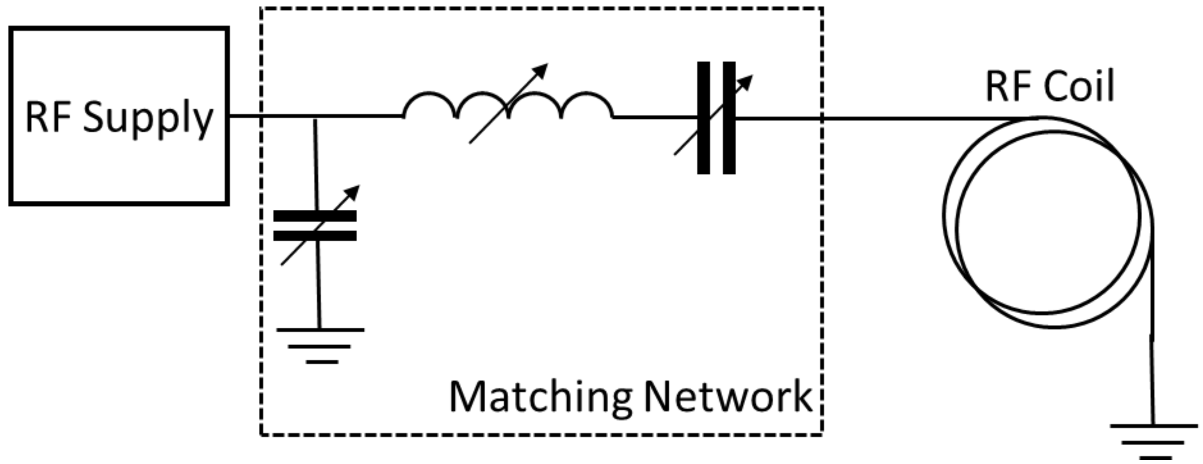


*Figure 5: Electrical circuit diagram detailing RF system.*

## 2.4 XRR Theory

X-Ray Reflectivity (XRR), is a used here for its application as a nanoscale, immediate-subsurface structural diagnostics tool that is sensitive to both film thickness and density. XRR functions by measuring the intensity of a grazing-incidence X-Ray beam reflected in the specular direction off of the sample.

The first feature of interest in the scan profile is the angle at which maximum reflection occurs, called the critical angle and represented as $\theta_c$, is directly dependent upon the density, $\rho$, of the film.

$$\frac{\theta_c^2}{\rho} = \frac{r_e \lambda Z N_A}{\pi A} = F \quad [5]$$

$r_e$ is the classical electron radius ($2.82*10^{-15}$ m), $\lambda$ is the x-ray wavelength, Z and A the atomic and mass numbers of the film, respectively, and $N_A$ is Avogadro's Number. [19] The product of these numbers, defined as F here, is then dependent upon only upon the known, material dependent constants, and specifics relating to the X-ray beam.

The second feature in the XR profile composes the majority of the spectrum, and essentially all of the spectrum beyond the critical angle: fringes. In the profile these appear as a pseudo-sinusoidal profile about an exponential intensity drop-off with respect to the scanning angle. Fringe

spacing is inversely linked to the thickness of the film, with thicker films having more tightly spaced fringes. Additionally, fringes provide information about the roughness of the surface and of any sub-surface structures. The angle out to which fringes are visible, as well as the rate of intensity drop-off of the exponential about which the intensity oscillates, correlate to the roughness of the surface and subsurface structures.

While there are strict mathematical relations between the features of the XRR spectrum and the physical constants in the ideal case, in general a model must be created and matched to the data in order to derive these physical properties.

## 2.5 Radical Probe Theory

Radical probes are thermocouples coated in a catalytic coating that enhances the recombination of the radical being measured. This recombination is an exothermic process, which provides a measurable temperature change. The difference in temperature between the catalytically coated probe, and a secondary control probe that is mounted adjacent to the first, can then be related to the density of radicals present in the vacuum system. [20] [21] [22] [23] Catalytic radical probes such as these are particularly useful as compared to other methods such as spectroscopic techniques as they do not require sight of the plasma, but can instead be mounted out of the way, relying on consistent diffusion of radicals throughout the vacuum system.

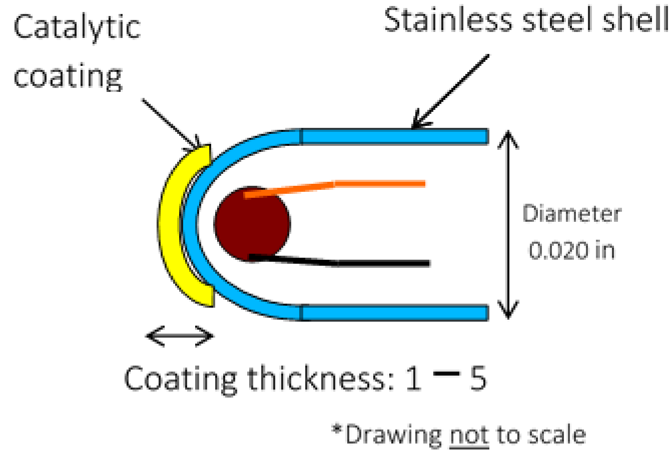


*Figure 6: Diagram of a catalytic radical probe. The Stainless steel shell (represented in blue, and the inner components represent the type K thermocouple used as a base. The catalytic coating is then applied onto the tip of the thermocouple, producing catalytic radical probe which measures the radical density by observing their catalyzed recombination rate.*

In detail, the derivation of the relation between the temperatures of the catalytically coated and non-coated control thermocouples and the radical density starts with considering the thermal steady-state heating and cooling rate of the thermocouples, which woks as follows:

$$\frac{nW_D vA\gamma_{Probe\,1}}{8} = \frac{S\chi}{l}(T_{cold,Probe\,1} - T_{hot,probe\,1}) \quad [6]$$

Where $W_D$ is the energy per recombination, n is the radical number density, v is the velocity of the radicals, A is the surface area of the probe, $\gamma$ is the recombination coefficient of the radicals on the surface of the probe (whether catalytically coated or not), S is the cross-sectional area of the probe, l is the length of the probe, and $\chi$ is the thermal conductivity of the probe. Taking this equation for both the catalytically coated and non-coated probes, which for the sake of simplicity should be equivalent except for the catalytical coating, and making the assumption that the cold, outer temperatures of the probes are identical, one can then derive the following expression.

$$n = \frac{8S\chi}{W_D vAl}\frac{T_{probe\,1} - T_{probe\,2}}{\gamma_{probe\,1} - \gamma_{probe\,2}} \quad [7]$$

Which allows for calculation of the radical density, as a function of the temperature difference between the probes. Other values, such as the surface recombination coefficients, need be determined from literature.

# 3. Setup/Methodology

## 3.1 Experimental Setup (SHADE)

### 3.1.1 Vacuum Chamber SHADE

The Sputtering High-purity Atomic Deposition Experiment (SHADE) is the vacuum system used for the depositions in this project. It features dual, side-by-side 4” Kurt J Lesker TORUS magnetron setup, with a sample holder that can be rotated through its central axis which points towards the magnetrons, as well as being movable along this axis. Samples can be loaded through a load-lock chamber, and moved into the main sample holder via a transfer arm. The Mo target (¼” thick, >99.9999% pure, purchased from Kurt J Lesker) mounted magnetron was initially powered by an Advanced Energy Power supply controlled by a MDX-052 Controller and, after this power supply failed irreparably, was replaced by a MagnaPower DC Supply. Working gas and pressure for all Mo depositions was 1.5 mTorr of Ar, with one exception where 0.5 mTorr $H_2$ gas was added to gauge the effects of $H_2$ gas on the deposition rate of Mo.

Si deposition was performed using a 1/8” thick, undoped Si target (>99.9999% pure, also purchased from Kurt J Lesker). Initial tests were performed using the same MDX power supply used to deposit Mo initially, until a second power supply, a Bertan Series 105 Power Supply, was procured to allow for later side-by-side deposition of the two materials on their individual magnetrons for the purpose of depositing multilayers. The working gas pressure for all regular Si depositions was 1.5 mTorr Ar, with $H_2$ added for attempts at hydrogenated Si as the experiment called for. Substrates used for deposition were cut from 6” diameter, undoped single crystal Si wafers, procured from MOMS Engineering & Material.

The main chamber is pumped by a turbomolecular pump (Osaka Vacuum Model TG800FCAB), which is backed by a rough pump (Osaka Vacuum Model DSP250). The load lock

chamber is pumped by a separate rough pump (Welch Model 1397). The main chamber additionally features a two separate halogen "bake out" lamps. The main chamber was habitually evacuated down to below $5.0*10^{-7}$ Torr ($6.7*10^{-5}$ Pa). Additionally, the magnetrons feature inverted magnetic configurations, providing a linked magnetic field loops (see schematic). Lastly, an ICP coil, intended for the generation of a secondary RF plasma discharge, is located approximately centered upon the sample holder, and above the sample. RF power is provided by a Kurt J Lesker R-series RF power supply, and is channeled through an L-type matching network with a 64-232 pF variable Shunt capacitor, a 22-61 pF variable Parallel capacitor, and a 0-17 $\mu$H variable inductor.

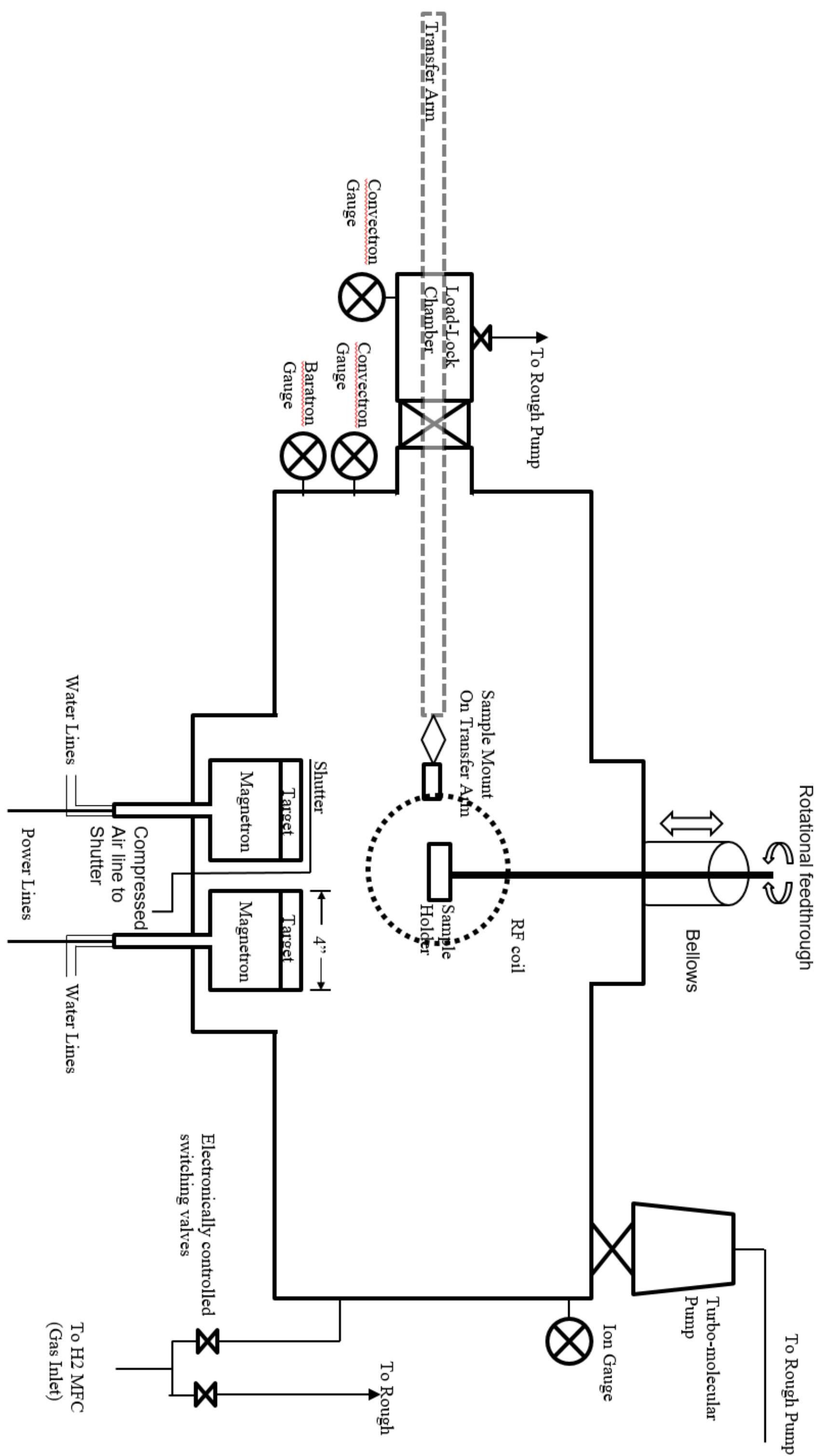


*Figure 7: Detailed Diagram of SHADE. RF Coil is located approximately 15 cm above sample holder. Magnetron to Sample Holder distance is approximately 7 cm.*

*Figure 8: Head on view of side-by-side Magnetrons and Shutter. In the foreground can also be seen the Quartz-Crystal Microbalance (QCM) which was left in the chamber in case its use became desired.*

Figure 8 is an image of the shutter and both side-by-side magnetrons in SHADE. The magnetron seen on the right of the image contains the Mo target, whereas the magnetron hidden behind the shutter bears the Si target. At the bottom of the left magnetron can be seen the shutter mechanism, a standard piece of kit sold by Kurt J. Lesker which is vacuum compatible and pneumatically activated. In the foreground can be seen a single, water-cooled Quart Crystal Microbalance (QCM), facing the Mo targeted magnetron, which, while not used, was left in the chamber in case its use became desired. Not pictured here is the sample holder, as the flange it mounts on was removed to allow for the taking of this image.

*Figure 9: Image showing view from the magnetron side. Shows the sample holder, QCM, ICP coil (coated in fibre-glass tape) at the top, and transfer arm connected to movable sample holder insert coming in from the left.*

In figure 9, an image showing the view in the main chamber from the magnetron side. In the center is the main sample holder, with the sample transfer holder partially slid out of it, and being held by the transfer arm. Behind this can be seen the water cooled QCM, which is partially obscured by the sample transfer holder. At the bottom left of the image can be seen a highly reflective metal cover that has been repeatedly cleaned of deposited materials, which covers one of the two halogen bake out lamps in the chamber. As can be deduced, the purpose of the cover is to ensure long term operability of the lamp despite being used in a deposition system.

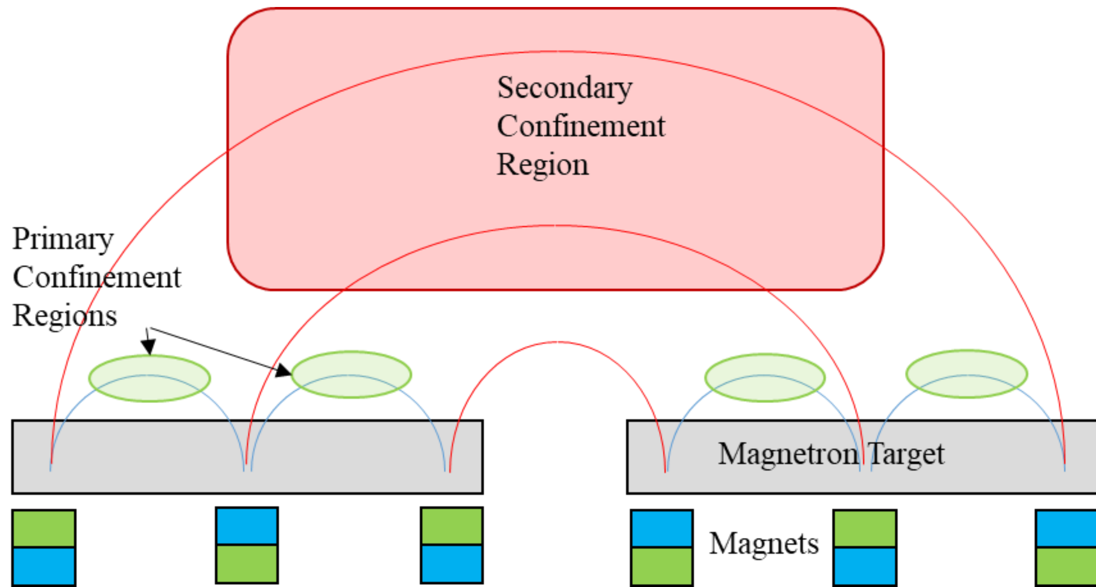


*Figure 10: Diagram of inverted/ closed loop magnetic flux configuration. Blue/Green rectangles indicate magnets with polarity as indicated by the colors. The small blue semi-circular lines indicate the standard magnetic flux found in any magnetron, with the green ellipses indicating the race track regions. The red field lines represent the secondary, longer range magnetic field lines that cross between the magnetrons.*

Figure 10, above, demonstrates the concept of the inverted magnet packs in a twin magnetron setup. In addition to the high strength fields close to the magnetron surface, the imbalanced/inverted magnet packs will generate a secondary field of lesser strength that goes from one magnetron to the other, providing a secondary area for (looser) confinement of a plasma, which stretches between the two magnetrons. This confines the secondary plasma, ensuring H radical/ion presence close to either magnetron (when $H_2$ gas is present) as well as in the intervening area.

### 3.1.2 LabVIEW Control Program

LabVIEW, Laboratory Virtual Instrument Engineering Workbench, combines a visual programming language with an easy to build frontend UI for created programs and easy communication with LabJack for computer controlled external mechnisms. LabVIEW is used here for two separate sets of controls.

The first is a simple control program which controls both the magnetron shutter and the $H_2$ gas flow fast response on/off valves. The program is set up to allow for either manual or automated control over both the shutter and $H_2$ flow. The program is connected via LabJack to three on/off gas valves which are supplied with pressurized air, and which automatically relieve pressure when shut off. The first of these valves is connected to the shutter and permits for movement between the shutters two distinct positions covering each magnetron. The two other lines hooked up to the program are connected to the pneumatically controlled fast switch on/off valves which are placed in between the $H_2$ MFC and either the chamber, or a separate vacuum line.

For automatic operation of the shutter and $H_2$ switching valves the program allows for the input of number of cycles, length of each of the two shutter dwell times, as well as a "late start" and "early shutoff" for the $H_2$ gas flow. This second component was included to ensure that all $H_2$ gas has been evacuated from the chamber by the time Mo begins deposition. This is done to ensure no hydrogen is incorporated into the deposited Mo layer, as well as to mimic the 'capping layer' of non-hydrogenated Si seen in similar work. [24]

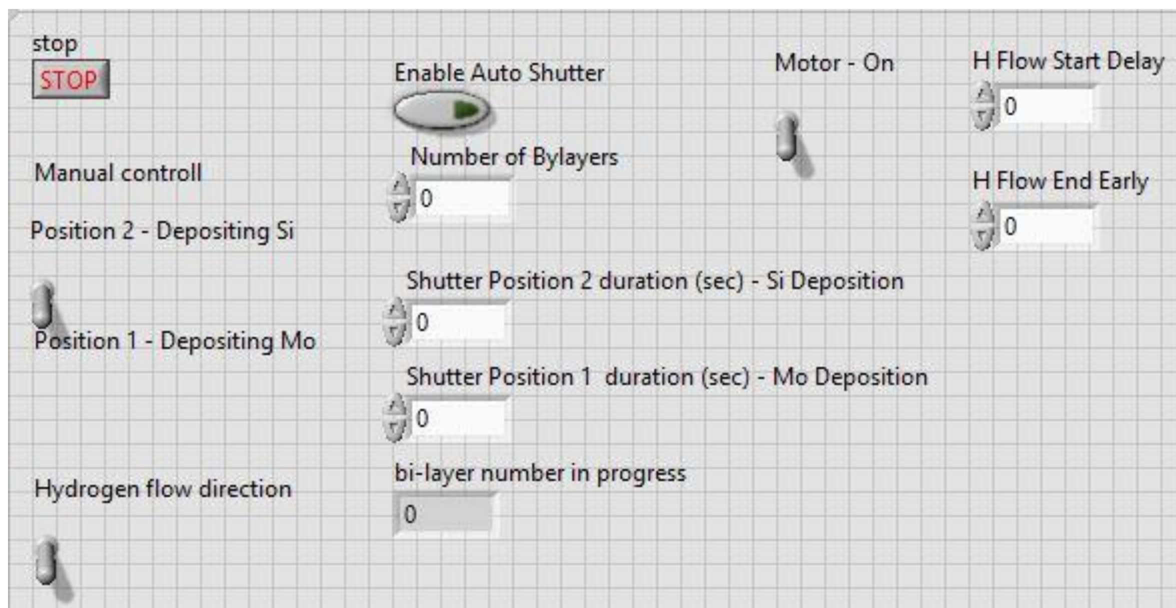


*Figure 11: Front-end UI of LabVIEW Control program for shutter and $H_2$ flow control. "Motor - On" switch was initially included for the purpose of computer controlled motor for substrate rotation, and was left in the program even after attempts to use it ceased, in case future experiments call for it.*

The second LabVIEW program that is used is a Radical Probe control program which automatically calculates radical densities when appropriately set up with radical probes. For details on the RP control program refer to Dren Qerimi's Master's Thesis (Title and publication to be determined).

## 3.2 XRR Data Collection and Modelling

### 3.2.1 XRR Data Collection

X-Ray Reflectivity (XRR) Data was collected using a PANalytical X-ray diffractometer, using a Copper K-alpha 1 X-ray source operated at 45 kV and 40 mA. The detector installed on the instrument was a PIXcel High Speed Line detector capable of 25 million counts per second per strip. The beam was constrained with a 1/32 degree divergence slit in the beam optics.

A note is made here relating to the behavior of the x-ray spectrum measured and the ideal case: at angles less than the critical angle, in the ideal case, the intensity should be constant as a constant amount of X-rays are reflected at these angles, which are typically $\theta \leq \sim 0.5°$. In reality due to the grazing angle significant portions of the X-ray beam are not reflected off of the sample surface as they cross the plane of the sample outside of the samples dimensions. This is referred to as the footprint effect, and is one of the main factors preventing a clear determination of the location of the critical angle.

### 3.2.2. What is IMD?

Modelling is done utilizing the IMD software, running on the X-Ray Oriented Programs framework [25]. IMD is a software for the modelling and analysis of multilayer films. It permits free manipulation of the structure being modelled, as well as the inputs and outputs. The software is produced by Reflective X-ray Optics and can be found at http://www.rxollc.com/idl/. [26]

### 3.2.3 Conversion of Data formats

One noteworthy consideration mentioned here is the method of converting the raw data output by the instrument into data usable by the program. The data output by the XRR device used can be saved as either counts or counts/sec, and is saved in a .xrdml format, whereas IMD reads tab delimited text files, and works best with data normalized to a maximum of 1. Additionally, the data is output with x-axis values of $2\theta$, the angle between the detector-sample line and source-sample line, where the sample is turned to half this angle to ensure reflection in the specular direction. The conversion then involves importation of the raw data into a spreadsheet program of choice, division of the angle by a factor of two, and normalization of the counts/sec data. Initially, the procedure used for this was an initially intuitive approach: first setting the pre-critical angle peak of the data to 1, and then scaling it down to match the model exactly. This yields a clean

matchup between the model and the data which, intuitively, appears good. However, a more appropriate and systematic approach was eventually introduced: In the XRR data, one can see a maxima at an angle of zero, with a minima before the eventual peak, after which occurs the critical angle. This peak at an angle of 0 corresponds to, assuming the instrument was properly aligned before taking the data, half of the maximum intensity of the X-Ray beam, as a half is permitted to pass by the sample at a zero angle and directly go into the detector, with the other half blocked completely. Setting this peak then, to a value of 0.5, is a more systematic method of scaling the data. It is worth noting that this may lead to an overestimation of the roughness of the sample, if one models the data with an intent of matching up the model and data magnitudes at higher angles.

### 3.2.4 Single Layer Modelling

Modelling of the XRR data is a fairly straightforward process, constrained more by the judgement of the individual modelling the data than anything else. A standard process for the modelling of the single layer is described here, which was generally followed, with modifications consisting only of the number of passes through the stages detailed here. Initially, after importing the data in IMD, the basic structure of the sample is defined. This is done by taking into account the deposition process for the sample in question, i.e. if it is known that the sample in question is a single Si film with a Mo contrast layer, then the basic structure is defined as a stack of bulk Si substrate, with a native oxide layer of approximately 3 nm on top of it. Above this is the Mo contrast layer which, due to pre-existing knowledge is generally set to an initial value of 1 nm thickness, and 9.8 ± 0.5% g/cm$^3$, a density value determined from previous Mo depositions. Then comes the Si layer in question, and finally an oxide layer is added to the model, though this is not

always used in the eventual fitting. If it is not deemed necessary, i.e. it does not provide any useful impact upon the model, then it is left at zero thickness.

Now that the basic model is defined, comes the initial pass of thickness of the film in question, as well as the density. In the case mentioned before, that of a single Si layer with a Mo contrast layer, this would provide four basic parameters in the first pass: Mo layer thickness, Si Layer thickness, and Si density. Layer thickness impacts primarily the spacing of the fringes while the density of the dominant film defines the location of the critical angle. This specification, that the density of the dominant film defines the location of the critical angle is the main reason for the restriction of the contrast layer to a small, approximately 1 nm thick Mo layer, instead of a thicker Mo film, as a thicker Mo film will drown out the signal from the Si film, regardless of its thickness (at least within the range of thicknesses considered here).

The initial pass aims not to finalize these values, but to provide rough estimates thereof, to enable the more accurate modelling of these values themselves in the second pass and onward. After the first pass across these variables, a second pass helps refine them and, if it is deemed necessary, this is repeated a couple of times until the model is deemed generally correct for thickness and density, if not yet roughness.

Next, as the previous paragraph hints at, comes the modelling of roughness, as the primary extraneous factor, though the instrument resolution is usually checked at this point as well, and is consistently found to be 0.008 degrees. The effect of roughness on the model depends on the layer the roughness is applied on, layers further down in the structure tend to affect the drop off in intensity with higher angles, whereas the roughness of layers close to the surface tends to affect the number of fringes observed, as well as the intensity scale difference across the fringe (i.e. “height amplitude” of the fringes). The instrumental resolution has an effect on the model similar

to that of the more surface layer roughness. Roughness' of all layers are can be considered, with some having more of an impact than others, potentially leading to the roughness of some layers being comparably insignificant to the model. In the example mentioned before then the roughnesses of consideration would be those of the Si wafer, native oxide layer, Mo layer, Si layer, and Si-oxide top layer. Worth mentioning is that the oxide thickness is dependent not merely on the specifics of the deposition, but also on the time the sample spent outside of vacuum between deposition and the XRR scan. While the native oxide layer on a Si film is self-terminating at 3-5 nm, the native oxide layer which forms on Mo is not self-terminating, and may grow significantly if the sample characterization is delayed by more than a day.

Once the roughness has been satisfactorily determined, an iterative approach between the density, thickness, and roughness is taken in the modelling, with variables that exhibit minimal effect being disregarded as the model is refined.

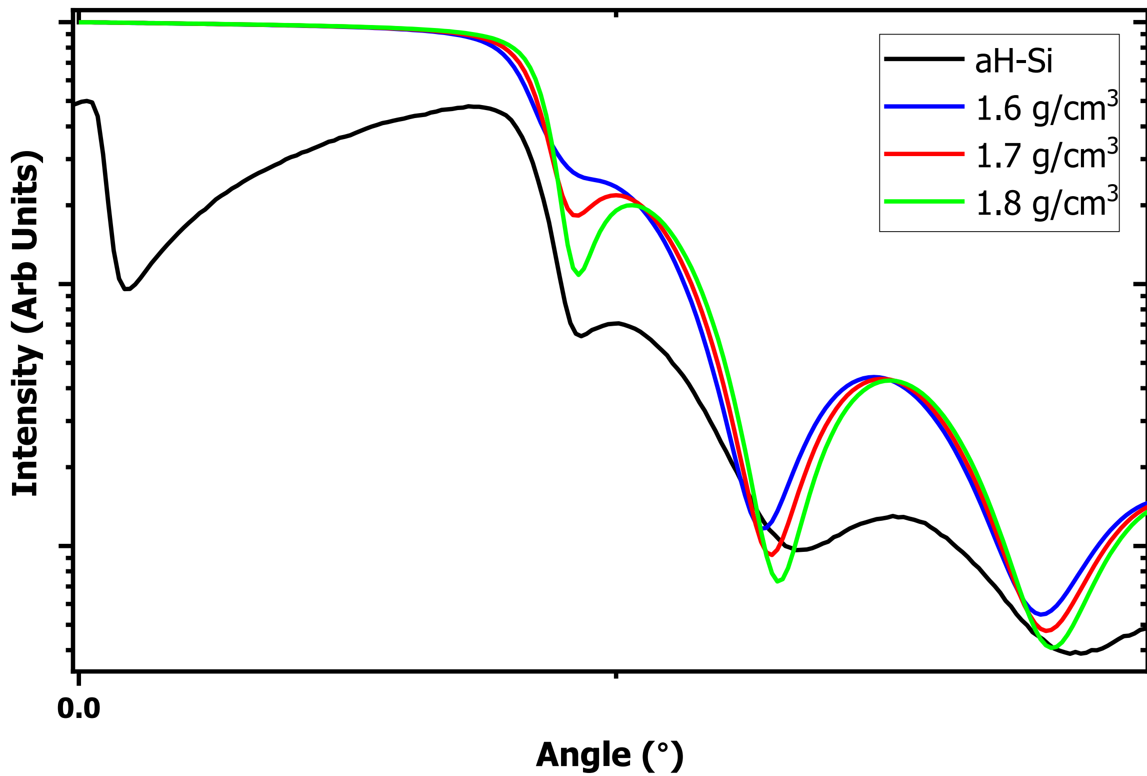


*Figure 12: Example of the model to data comparison during the first density determination of a single Si:H film. The curve in black, seen at the bottom, is the data itself, while the three curves above it correspond to models with the only variable being differing densities: Blue [1.6 g/cm$^3$], Red [1.7 g/cm$^3$] and Green [1.8 g/cm$^3$]. In modelling of this data 1.7 g/cm$^3$ was chosen as the most appropriate after due deliberation.*

Above is an example of intermediate step when fitting XRR data, namely a first rough density fit. In red is the actual XRR data, with the three other curves for varying densities with all other factors held constant. In this image it can be seen that, while the indicated intensity is not entirely accurate, the fringe spacing and location of the critical angle are, approximately, correct for all three, with minor differences in the fringe location due to the varying density based critical angles. It is then the job of the individual modelling the data to determine which of the curves matches the data best. In this case, the location of the critical angle, as well as the shape of the first fringe minima indicates that the green curve (corresponding to a density of 1.6 g/cm$^3$) is incorrect. This leaves the other two options: 1.7 g/cm$^3$ (blue) or 1.8 g/cm$^3$ (orange). The conclusion drawn at this stage was that the blue line appeared to have a closer resemblance to the actual data, due to the

shape of the first fringe, but certainly neither was entirely accurate. The eventual conclusion for this data set was a density of 1.73 g/cm$^3$.

### 3.2.5 Multilayer Modelling

The other side to consider is then the modelling of the multilayer. In doing so, different characteristics must be addressed. First, in preparation for modelling, the expected densities of the Mo and Si film must be established from single layers, the reason for this, as opposed to attempting to derive the densities of the Mo and Si layers from the Multilayer model. The reason for this comes from the fact, that the two main variables that are tuned in the multilayer model, are the bilayer thickness, d, and the bilayer ratio, Γ. To remind the reader: the term "bilayer" in this context refers to the combination of a Si and Mo layer that, in the structure of the multilayer, form the periodic building block the entire multilayer is constructed from. "d" represents the thickness of the bilayer itself, with the total thickness of the sample then being N*d, where N is the number of bilayers present. Γ is the ratio of the thickness of the "bottom" layer in the bilayer, to the thickness of the entire bilayer.

Similar to the modelling of a single layer, a standard process was established for the modelling of a multilayer. In the modelling of the multilayer, N is a variable that can, if the multilayer stack and by extension the XRR data are sufficiently clean, be determined from the data. In general it is also trivially defined from the deposition process, where the number of bilayers to be deposited is an input variable. d and Γ are then the two main variables to model, with the combination thereof indicating the layer thickness of both the Si and Mo layers present in the multilayer stack. The bilayer thickness, d, affects the spacing of the major and minor fringes in the model, as would be expected from the behavior of the fringe spacing vs thickness observed in a single layer model.

The ratio, Γ, meanwhile affects a multitude of factors at once, with the two primary factors being the relative heights of the major peaks, as well as the critical angle observed for the multilayer. Additionally, the density of the individual films affects these same indicators, and it is for this reason that the density of the films must be an input variable that is previously determined. As was alluded to before, in a clear multilayer XRR profile, N, the number of bilayers, determines the number of minor fringes present between the major fringes. In general, or at least for the purpose of this document, some of these minor fringes are often lost due to the roughness of the layers, or other problems, and therefore N cannot always be perfectly determined, though as it can be treated as a fixed variable determined from the deposition conditions, this is not a problem. Finally, the roughness, both within the multilayer stack, and on top of it, as well as the roughness of the underlying wafer and native oxide, are to be modelled and act much as they do in the case of a single layer. One thing to be careful with while manipulating the roughness of the layers in a multilayer is that due to the comparable thickness of the individual layers, the range of permitted roughness is far smaller.

## 3.3 Radical Probe Manufacture and Installation

Radical probes used in this experiment were created using K-Type thermocouples, gold coated via a goldplating.com "Goldsmith Gold Plating Kit", in conjunction with 24K Brush Gold Solutions, also from goldplating.com. For the collection of data a single catalytically coated thermocouple is placed side-by-side with a single non-coated thermocouple which acts as the control. The connections were connected to a standard, Kurt J. Lesker K-Type Thermocouple Feedthrough on a 2 ¾" CF flange, and placed on a flange in the same plane as the magnetron water

and power connections. The radical probes were then settled in between the magnetrons, sitting on top of them, and held in place using Kapton tape.

## 3.4 AFM

Atomic Force Microscope (AFM) data was collected using an Asylum Research MFP-3D™ AFM tool, in conjunction with Budget Sensors BS-Tap300Al tapping tips, which provides a lateral resolution of approximately 8 nm when the tips are new. All measurements were performed in tapping mode. Image processing, surface roughness measurements, and other analyses were performed using the Igor Pro software package which controls the AFM.

# 4. Results and Discussion

## 4.1 Mo Films

| Code | Power Supply | Setpoint | Dep Time (h:m:s) | Ar Pressure (mTorr) | Mo Thickness (nm) | Density (g/cm^3) | Deposition Rate (nm/min) |
|---|---|---|---|---|---|---|---|
| M11_A | MDX | 0.5 A | 0:05:00 | 1.5 | 53 | 9.7 | 10.600 |
| M12_A | MDX | 0.25 A | 0:05:00 | 1.5 | 24 | 8.7 | 4.800 |
| M14_A | MDX | 0.25 A | 0:02:00 | 1.5 | 17 | 6.3 | 8.500 |
| M15_A | MDX | 0.5 A | 0:02:30 | 1.5 | 26.3 | 9.7 | 10.520 |
| M16_A | MDX | 0.5 A | 0:01:15 | 1.5 | 12.9 | 9.7 | 10.320 |
| M20_A | MDX | 0.5 A | 0:00:38 | 1.5 | 6.5 | 9.7 | 10.263 |
| M24_A | MDX | 0.5 A | 0:05:00 | 1.5 | 50.2 | 9.7 | 10.040 |
| M35_A | Magna | 0.25A | 0:05:00 | 1.5 | 51 | 9.8 | 10.200 |

*Table 1: Tabulated Mo film data*

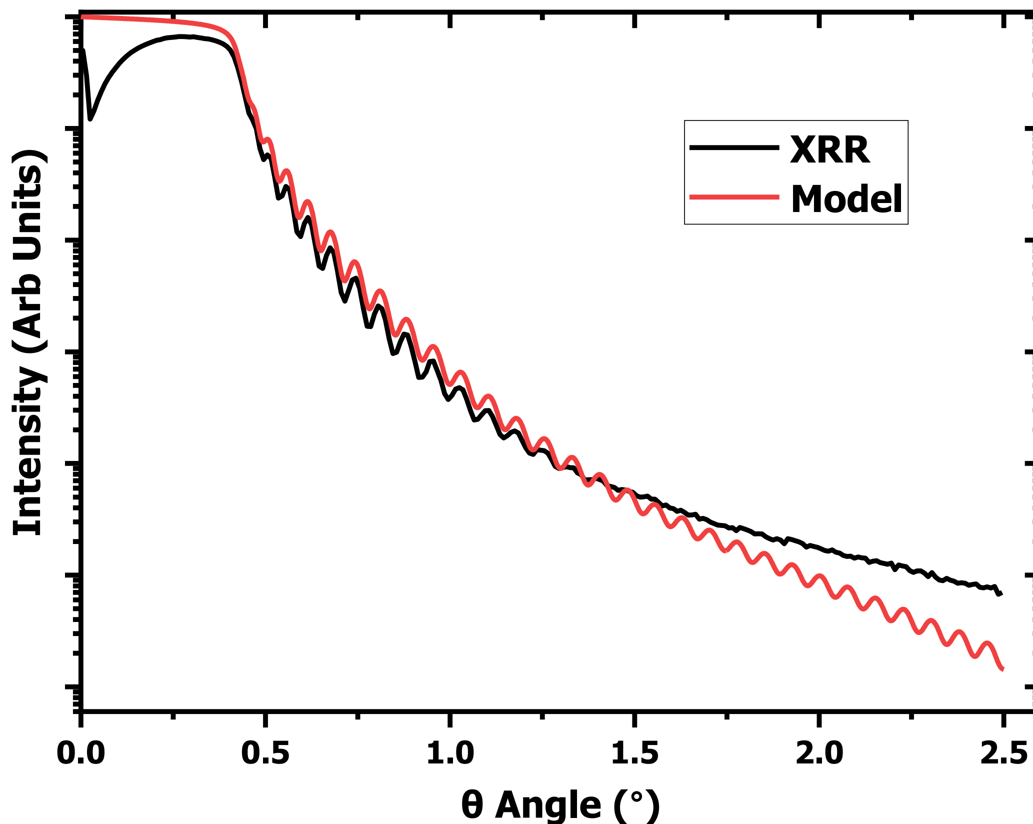


*Figure 13: XRR Data and Model for a 51 nm thick Mo film (M11_A). fitted primarily for density (9.8 g/cm3) and thickness, leading to critical angle matchup and fringe spacing matching that are acceptable. Clearly demonstrates footprinting effect seen at angles below the critical angle. Limitation of this model likely to be overestimation of roughness of lower layers, due to drop off of the model intensity at higher angles compared to the raw data. Additionally, the roughness of surface layers is likely under-estimated, due to presence of fringes in model far in excess of that seen in the data.*

The Mo films were deposited on square, single crystal Si substrates, 2.5 cm a side. Characterization was done utilizing XRR, an example can be seen above. Deposition setpoints were initially varied, with the two initially most promising setpoints on the MDX having been 0.25 and 0.5 A. Both of these setpoints showed initial promise due to the recorded deposition rate, however the 0.25 A setpoint, as can be seen from the table above, produced inconsistent results both in dep rate and density of the Mo. Additionally, the density value of both of these films appeared to be too distant from the standard, established density of 10.2 g/cm$^3$, and this combination lead to the adoption of the 0.5A setpoint for further use. It is worth noting that the density of the 0.5A setpoint produced films is reduced compared the literature value, with one likely reason being the non-ordered structure of the magnetron sputtered film. After the Advanced Energy Power supply failed and it was replaced with the MagnaPower, an initial deposition was performed using the same setpoint of 0.5A, which produced, over our standard characterization time scale of 5 minutes, a film that was far thicker than expected. The setpoint was therefore reduced to 0.25A and it was observed that this setpoint matched the AE power supplies deposition at 0.5A quite closely, indicating that the AE power supply may have had issues from the beginning of the project. A closer look at the insides of the power supply indicated that it had previously been modified in-house to some extent, and this seemed like a likely culprit for the discrepancy. While no study of repeatability was performed for the Mo only with the MagnaPower supply at the time, subsequent depositions of multilayers appeared to indicate that the deposition rate was repeatable. As a last side-note, the deposition of Mo in the presence of Hydrogen gas lead to an interesting phenomenon where the density was reduced by ~20%, while the thickness deposited increased by the same amount, indicating a net deposition of the same amount of Mo, just in a more porous form.

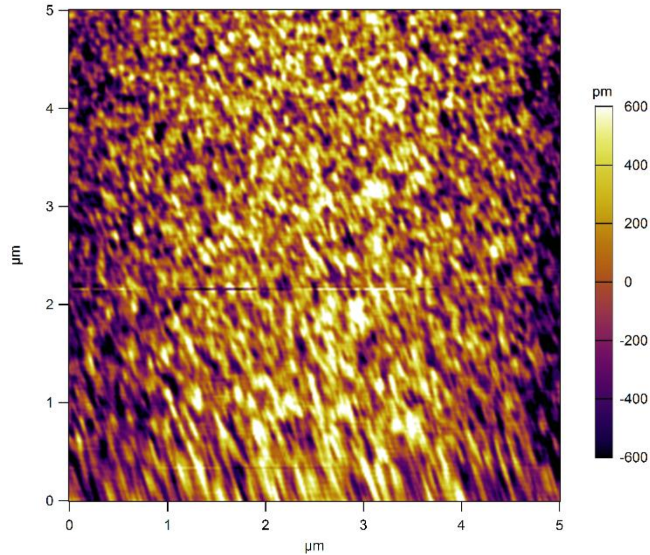


*Figure 14: AFM micrograph of a ~50 nm thick Mo film. The Streaking at the bottom of the image is due to variance in the tip drive amplitude and may be disregarded when determining film roughness. Clearly shows that the roughness of the Mo films produced is on the order of fractions of a nanometer, for a ~50 nm thick film, well within the acceptable range.*

Results obtained from the XRR were checked using AFM, with a particular focus on surface roughness. The above AFM micrograph belongs to an approximately 50 nm thick Mo film, with AFM indicating a roughness less than 0.25 nm. For comparison, XRR indicated a roughness of approximately 1 nm, reinforcing the previously mentioned belief that with the XRR modelling procedure followed the roughness is overestimated. The main take-away is that the roughness of the Mo films produced is well within acceptable limits.

## 4.2 Si Films

| Code | Power Supply | Setpoint | Si Dep Time (hh:mm:ss) | Ar Partial Pressure (mTorr) | Si Thickness (nm) | Density (g/cm^3) | Deposition Rate (nm/min) |
|---|---|---|---|---|---|---|---|
| S14_A | B105 | 75 mA | 00:05:00 | 1.5 | 43 | | 8.600 |
| S17_A | B105 | 50 mA | 00:05:00 | 1.5 | 19.1 | 2.2 | 3.820 |
| S19_A | B105 | 50 mA | 00:02:30 | 1.5 | 9.3 | 2.2 | 3.720 |
| S20_A | B105 | 50 mA | 00:01:15 | 1.5 | 4.5 | 2.2 | 3.600 |
| S21_A | B105 | 50 mA | 00:05:00 | 1.5 | 18.8 | 2.2 | 3.760 |
| S22_A | B105 | 50 mA | 00:10:00 | 1.5 | 38.1 | 2.2 | 3.810 |
| S23_A | B105 | 50 mA | 00:05:00 | 1.5 | 19 | 2.3 | 3.800 |
| S38_A | B105 | 50 mA | 00:07:36 | 1.5 | 28 | 2.2 | 3.684 |
| S43_A | B105 | 50 mA | 00:05:00 | 1.5 | 19.4 | 2.2 | 3.880 |
| S47_A | B105 | 50 mA | 00:05:00 | 1.5 | 16.9 | 2.2 | 3.380 |
| S51_A | B105 | 50 mA | 00:05:00 | 1.5 | 15.7 | 2.2 | 3.140 |
| S62_A | B105 | 50 mA | 00:05:00 | 1.5 | 19.2 | 2.28 | 3.84 |
| S78_A | B105 | 50 mA | 00:05:00 | 1.5 | 17 | 2.2 | 3.4 |

*Table 2: Tabulated collection of non-hydrogentaed Si film data points*

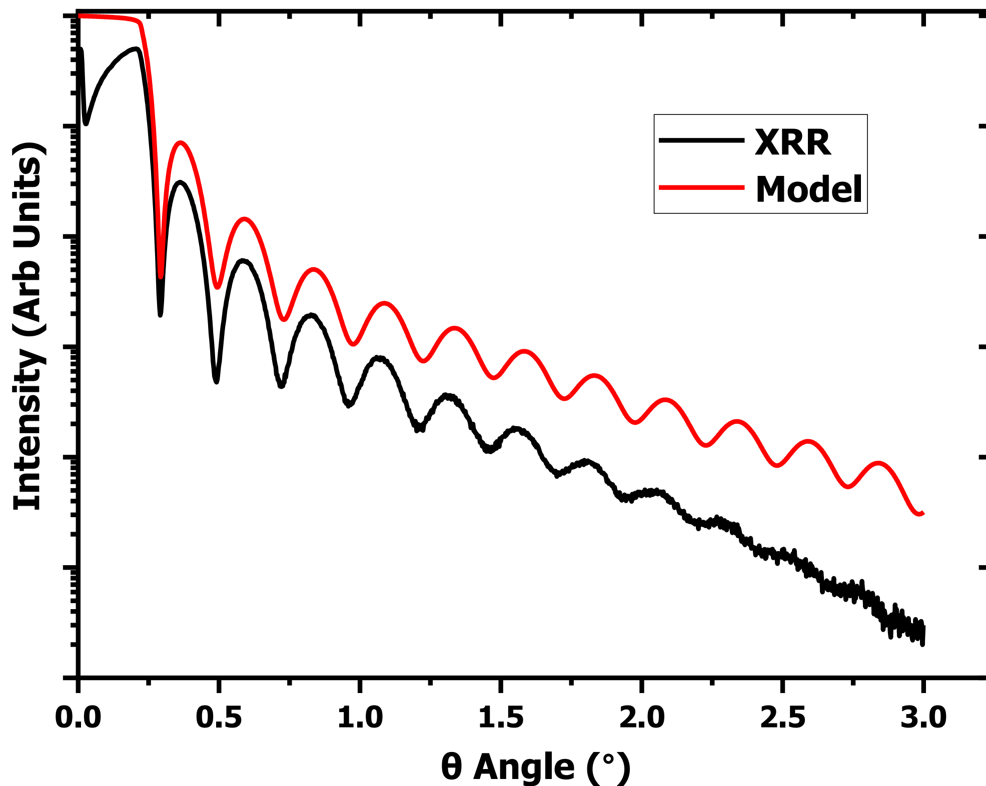


*Figure 15: XRR data and model for 17 nm thick Si film with a density of 2.2 g/cm$^3$ (S78_A). Fringe spacing and critical angle match well, indicating density and thickness are accurate. Roughness is likely to be slightly underestimated across the board, as indicated by reduced intensity drop off of model compared to data, as well as the presence of clear fringes out to larger angles in the model as compared to the data.*

As with the Mo films, all Si films were deposited on -square cut, single crystal Si substrates, 2.5 cm to a side. The primary difference here is that, in order for the XRR measurement to be sensitive to the deposited Si film, a roughly 1nm thick Mo film was deposited first as a contrast layer. Characterization was performed using XRR, utilizing this to determine the density and thickness, with a secondary effect of determining an estimate of the roughness in the process. Some variation of the setpoint for the Si depositions was performed initially, with a rapid move to a setpoint of 50 mA, which yielded a standard voltage of around 680 V. As can be seen from the table, the density that was fit to the XRR data generally came out to be 2.2 g/cm$^3$, as compared to the literature value of 2.33 g/cm$^3$, a potential indication that while reasonably clean Si, there is likely to be some oxides, as well as an amorphous, component to its structure. Deposition rate, meanwhile, was reasonably consistent, with some of the variation likely being explained by insufficiently thorough cleaning plasmas before deposition, which will reduce the initial rate as the native oxide is burned off of the target. It may well be worthwhile redoing a more thorough repeatability test of the Si deposition rate with thorough cleaning plasmas, however the only place where it is likely to make a significant difference is during the deposition of multilayers, where a thorough cleaning plasma step has been applied right before the deposition, eliminating the inconsistency there.

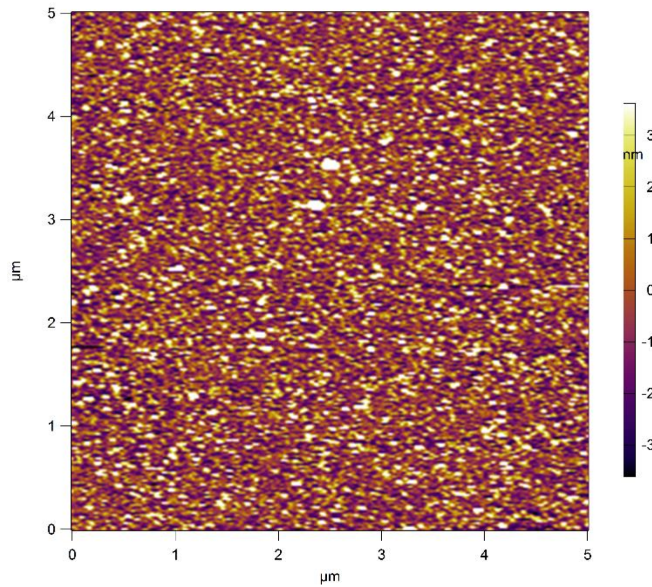


*Figure 16: AFM micrograph of a 20 nm thick Si film with a surface roughness of 2-3 nm. The two white spots seen at near the center of the top half of the image are most likely almost identical nanoparticles at 40 nm in diameter.*

Once again, the roughness of the film in particular needs be double checked via AFM. In this case the above AFM micrograph is for a 20 nm thick Si film, and indicates a surface roughness of approximately 2-3 nm. Surface roughness in the XRR data was modelled as ~1 nm, which, as opposed to the case for Mo, underestimates the actual roughness notably. While certainly not ideal, this roughness over a 20 nm thick film was deemed acceptable, if not ideal.

## 4.3 Si:H Films

| Code | Setpoint | Si Dep Time (hh:mm:ss) | H Partial Pressure (mTorr) | RF FWD [W] (Forward/Set RF Power) | RF REF [W] (Reflected RF Power) | Si Thickness (nm) | Density (g/cm^3) | Deposition Rate (nm/min) |
|---|---|---|---|---|---|---|---|---|
| S24_AH | 50 mA | 00:05:00 | 0.5 | | | 16.3 | 2.04 | 3.260 |
| S29_AH | 50 mA | 00:05:00 | 5 | | | 6 | 1.8 | 1.200 |
| S34_AH | 50 mA | 00:30:00 | 7.5 | | | 15.8 | 2 | 0.527 |
| S39_AH | 100 mA | 00:10:30 | 5 | | | 28.4 | 1.68 | 2.705 |
| S41_AH | 100 mA | 00:19:25 | 5 | | | 59 | 1.2 | 3.039 |
| S48_AH | 100 mA | 00:05:00 | 5 | | | 11 | 1.7 | 2.200 |
| S49_AH | 100 mA | 00:05:00 | 0.5 | | | 27 | 1.74 | 5.400 |
| S50_AH | 100 mA | 00:05:00 | 0.5 | 100 | 0 | 25 | 1.7 | 5.000 |
| S52_AH | 100mA | 00:05:00 | 0.1 | 92 | 50 | 31 | 2.1 | 6.2 |
| S53_AH | 100mA | 00:05:00 | 0.05 | 140 | 40 | 31 | 2.1 | 6.2 |
| S56_AH | 100mA | 00:05:00 | 0.3 | 235 | 35 | 29.6 | 1.96 | 5.92 |
| S57_AH | 100mA | 00:05:00 | 0.1 | 370 | 70 | 25 | 1.89 | 5 |
| S58_AH | 100mA | 00:05:00 | 0.2 | 365 | 65 | 17 | 1.83 | 3.4 |
| S59_AH | 100mA | 00:05:00 | 0.3 | 364 | 64 | 26 | 1.73 | 5.2 |
| S61_AH | 100mA | 00:05:00 | 0.3 | 127 | 27 | 32 | 1.91 | 6.4 |
| S67_AH | 200mA | 00:05:00 | 0.3 | 300 | 0 | 63 | 2.3 | 12.6 |
| S68_AH | 150mA | 00:05:00 | 0.3 | 300 | 0 | 12.4 | 1.7 | 2.48 |
| S77_AH | 100mA | 00:05:00 | 0.3 | 301 | 1 | 27.6 | 1.85 | 5.52 |

*Table 3: Tabulation of hydrogenated Si film data points.*

Initial trials for producing a hydrogenated Si film were attempted in the most simplistic manner possible: by the addition of a significant $H_2$ partial pressure into the working gas during deposition of the Si film. Early attempts maintained the deposition setpoint used to previously to deposit regular Si, a setpoint of 50mA utilizing the Bertan Series 105 DC power supply, while varying the $H_2$ partial pressure. Initial attempts were made using a $H_2$ partial pressure of 0.5 mTorr $H_2$, which lead to a notable, but less than desired decrease in the density of the aSi:H film, down to 2.04 g/cm$^3$ from 2.2g/cm$^3$, which was shown with sample S24_AH. The $H_2$ partial pressure was subsequently increased, while still maintaining the 1.5 mtorr Ar level, to a $H_2$ partial pressure of 5 mtorr. At otherwise identical conditions this lead to sample S29_AH, with a density of 1.8 g/cm$^3$, with the caveat that this sample was quite thin, coming in at only 6nm of thickness. As this was

approaching the lower limit of the usefulness of XRR, the deposition time for the next attempt was increased drastically to 30 min, as compared to the previous 5 min deposition durations. In combination with this change, and to see the extent to which our system could be pushed, the $H_2$ partial pressure was increased to 7.5 mtorr, which approached the limit of what could be achieved in the system, with the components installed. This attempt appeared to show no significant benefit beyond the previous deposition at 0.5 mtorr $H_2$, as S34_AH appeared to show a density of 2 g/cm$^3$, along with a severely reduced deposition rate (0.53 nm/min as compared to 1.2 nm/min for the initial 5 mtorr $H_2$ film).

With an initial rough scan across $H_2$ pressures completed, with some promising results for the 5 mtorr $H_2$ pressure, the decision was made to next modify the current setpoint at which the deposition was performed. The reasoning used to justify this change was the thought that, at a higher current setpoint, the plasma should increase in ion/electron density, which in turn should generate more H radicals and ions, leading to more H incorporation in the film. The current setpoint was therefore doubled, as compared to previous depositions, leading rapidly to sample S39_AH, which indicated a density of 1.68 g/cm$^3$. A promising result. Further trials were run at the 100mA current setpoint, with 5 mtorr $H_2$ partial pressure and 1.5 mtorr Ar used for S39, to confirm repeatability and scalability of the results. Among these scalability tests one particular sample

became of note: S41_AH, which, with a deposition time of 19 min and 25 seconds was the thickest aSi:H sample deposited at a thickness of 59nm.

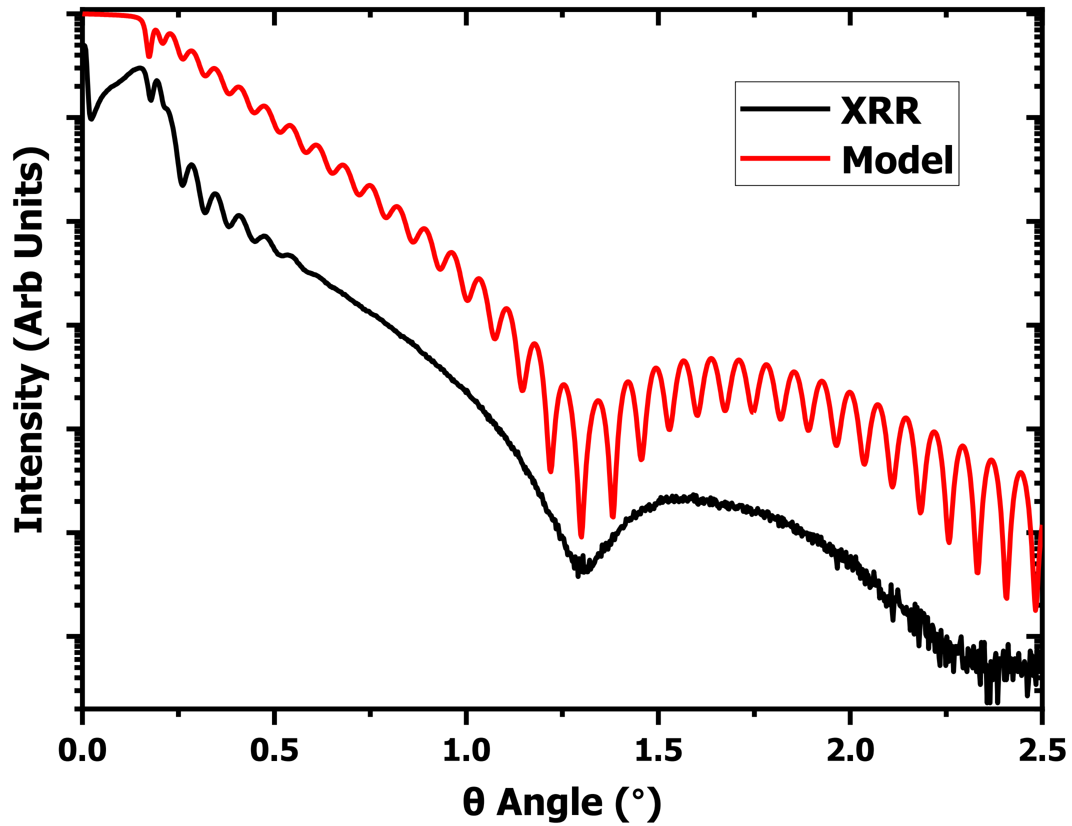


*Figure 17: XRR Data and Model for S41_AH. First indication of issues with the 5mtorr $H_2$ partial pressure films. Clearly the data shows non-standard behavior in the region surrounding the critical angle. The unusual appearance of this data set was the first indication as to there being an issue with S41_AH, with the fitted density of 1.2 g/cm$^3$, as compared to the expected 1.7 g/cm$^3$ from previous samples deposited at the same conditions but for shorter time periods, being the secondary indicator reinforcing the idea that a problem existed.*

However, this is not the main component that made this sample standout, instead, the XRR profile was quite unusual, and modelling thereof indicated a density of 1.2 g/cm$^3$. This, of course, is well outside the realm of what one might expect from sample to sample variation. After looking at the sample under the SEM, it became clear what the problem was.

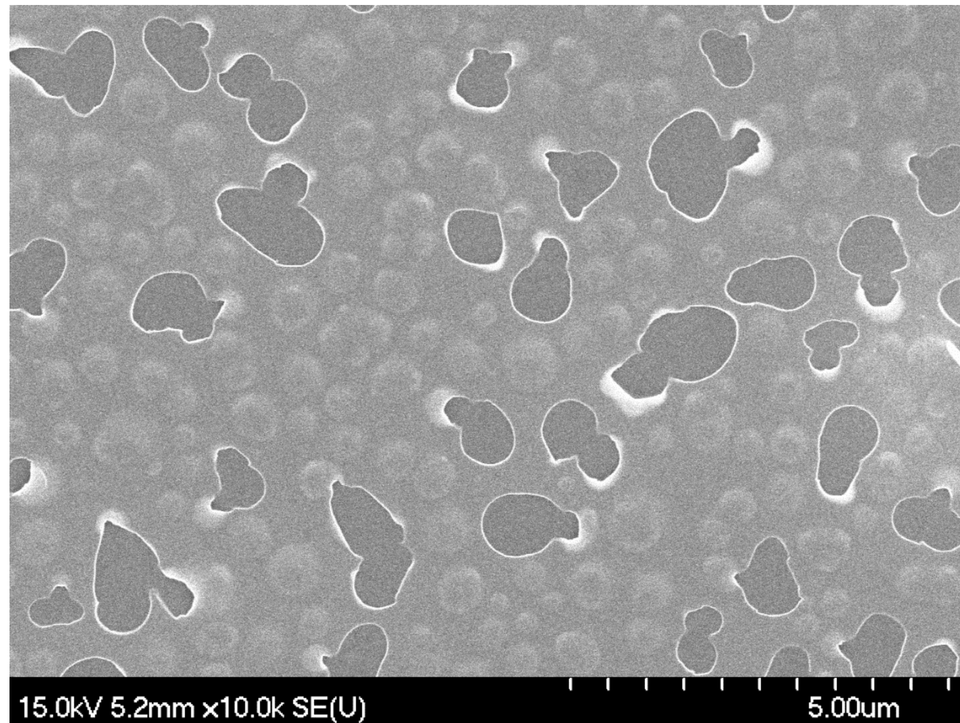


*Figure 18: SEM of S41_AH, for which the XRR was shown above. This SEM image was the first confirmation of the presence of areas of delamination, and the presence of some subsurface features which were assumed to be the reason for the delamination. While the theory of gas blisters was put forth from this image, confirmation thereof was found later with further characterization of this sample and others.*

As can be seen from the image above, there are clearly subsurface features, and areas where the film appears to be missing entirely. After thorough discussion, the most likely scenario that could explain these features was determined to be the formation of subsurface blisters or bubbles of $H_2$ molecules that have become trapped by the film. As the deposition continues, these blisters continue to grow and, eventually, produce enough stress on the film to cause the localized delamination of part of the film, optionally with enough bleed over into another bubble to cause the multi-bubble delamination that can be observed in the image above.

After this discovery, numerous previously deposited samples were analyzed with SEM, and in some cases AFM, in order to determine the degree to which this problem prevails, and also to see if any further insight could be gained into the veracity of the above indicated process of what occurred.

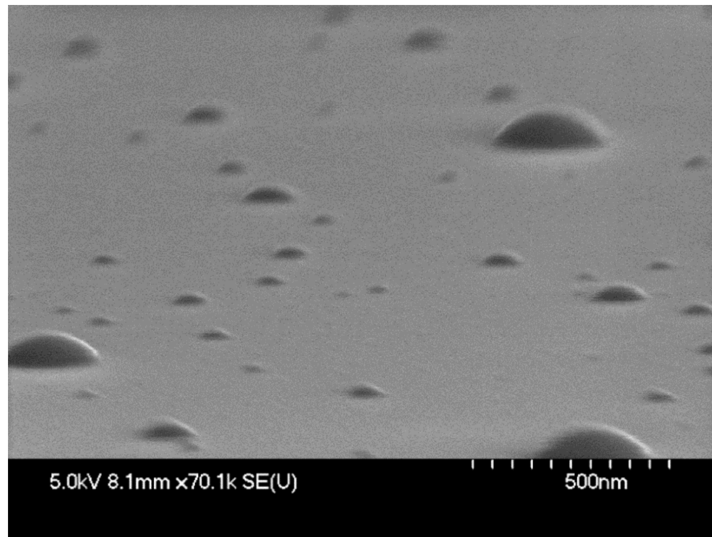


*Figure 19: 45 degree angels SEM of hydrogen blisters. Strictly, this image was the confirmation of the previously established theory that the surface features seen were blisters.*

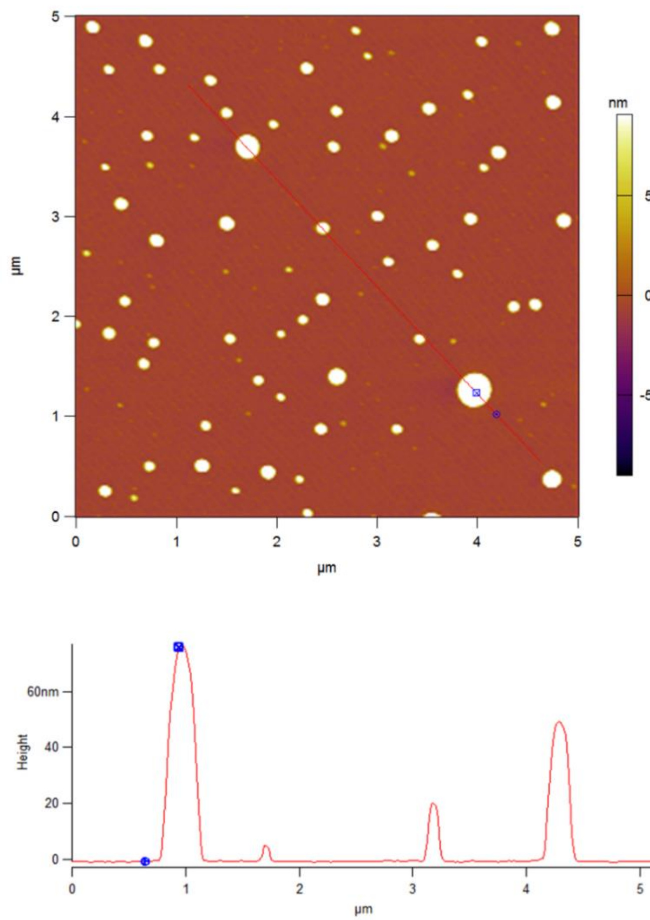


*Figure 20: AFM test across bubbles, confirming the shape and height ranges of the blisters. Clearer confirmation than a 45 degree angled SEM as to the existence of gas blisters in the film.*

Both figure 19 and 20 were taken during this period. One showing the 45 degree angled SEM view of the bubbles, and the second being an AFM trace across these bubbles. From these it can clearly be seen that the bubbles extend beyond the surface of the “smooth” part of the film, which is consistent with what would be expected from a blister that eventually produced sufficient stress to “pop off” a part of the film. An additional image, shown below, is curious as it shows the intermediate step, where cracking of the film begins to occur, but delamination has not yet occurred. It is worth noting that this last image is not of a single hydrogenated Si layer, but is instead from an early attempt of a hydrogenated, 20 period multilayer, which was deposited before the presence of the bubbles was detected in the single Si:H films. This multilayer structure is likely the cause for the crack occurring across the edge of an area with many smaller bubbles in it, with the likely explanation being that as the multilayer continued to be deposited the bubbles formed at multiple interfaces within the multilayer structure.

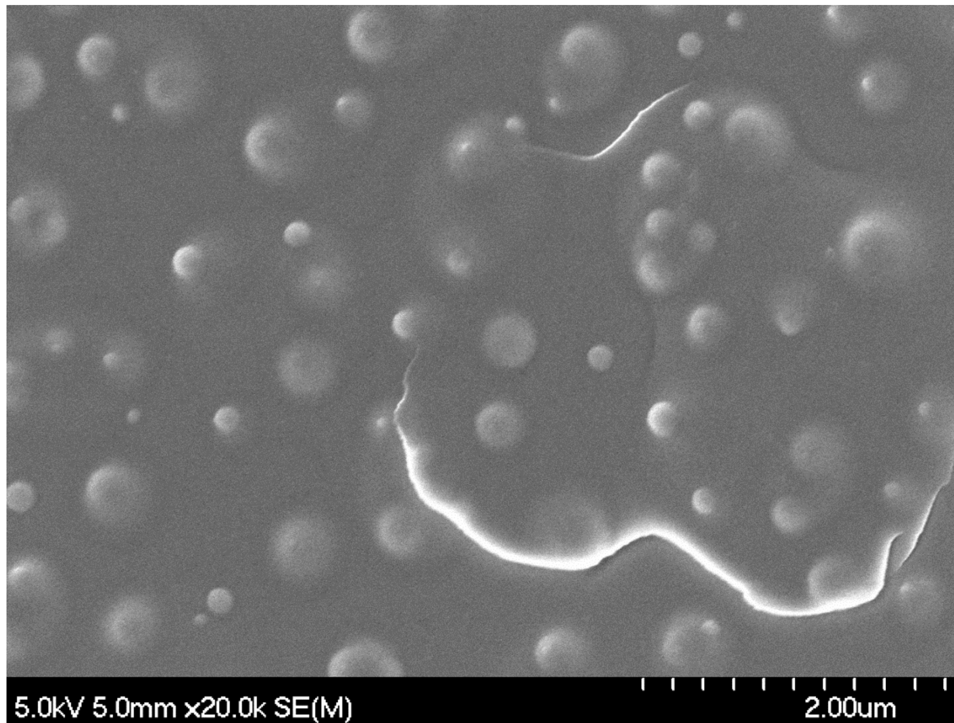


*Figure 21: Example of cracking occurring in the film, but not yet delamination. Useful for indicating that the previously held assumption that the blisters are responsible for the delamination is likely correct, without being able to directly observe the phenomenon in-situ.*

Assuming that the proposed method for the reason for the presence of the bubbles is correct, namely the capture of non-bonded (to the film) $H_2$ molecules by the film, a solution, and the solution that is investigated here, is comparatively straight forward: the use of a secondary RF plasma for the generation of an increased number of H radicals or ions, which are more reactive and, when bound in the film, are expected to stay in place in the film. In addition to the inclusion of a secondary RF plasma the $H_2$ partial pressure was reduced in order to reduce the number of $H_2$ molecules present.

Initial tests were run at 100W of RF power, and 0.5 mtorr $H_2$. This sample, S50_AH, had a density of 1.7g/cm$^3$, however was found to still have bubbles present. The next samples were deposited at $H_2$ pressures as low as could be achieved in the system, together with 100W RF plasmas. S52 and S53 were the result, at 0.1 and 0.05 mtorr $H_2$ respectively. Neither indicate much hydrogen incorporation, both being modelled with a density of 2.1 g/cm$^3$. Due to the similarity of

these results, and the difficulty of generating a 0.05 mtorr $H_2$ partial pressure in the system lead to investigation of the 0.1-<0.5mtorr $H_2$ realm, along with varying higher RF Powers. 0.1, 0.2, and 0.3 mtorr $H_2$ levels and 100, 200, and 300W RF Power levels were investigated. The results are shown in the table below.

| **Density ($g/cm^3$)** | | **$H_2$ Pressure (mTorr)** | | |
|---|---|---|---|---|
| | | 0.1 | 0.2 | 0.3 |
| **RF Power (W)** | 100 | 2.1 | - | 1.91 |
| | 200 | - | - | 1.96 |
| | 300 | 1.89 | 1.83 | 1.73 |

*Table 4: Densities of hydrogenated silicon films at varying $H_2$ partial pressures and RF powers. Missing values are for films which were deposited had problematic XRR scans, prohibiting useful modelling.*

The blank spaces left in this table were all deposited, however, the XRR for these samples was less than clean, providing no useful information. Based on these, the roughly expected picture emerges: density decreases, both with an RF power increase, or a $H_2$ pressure increase. Initial SEM scans were taken of the 0.3 mTorr $H_2$, 300W RF Power sample (Sample S59_AH), which appeared to indicate no presence of blisters, merely the presence of some dust/etc. The particular image shown below shows the only feature that was found on this sample that appeared to be reminiscent of the blisters seen previously, and it still appears quite distinct.

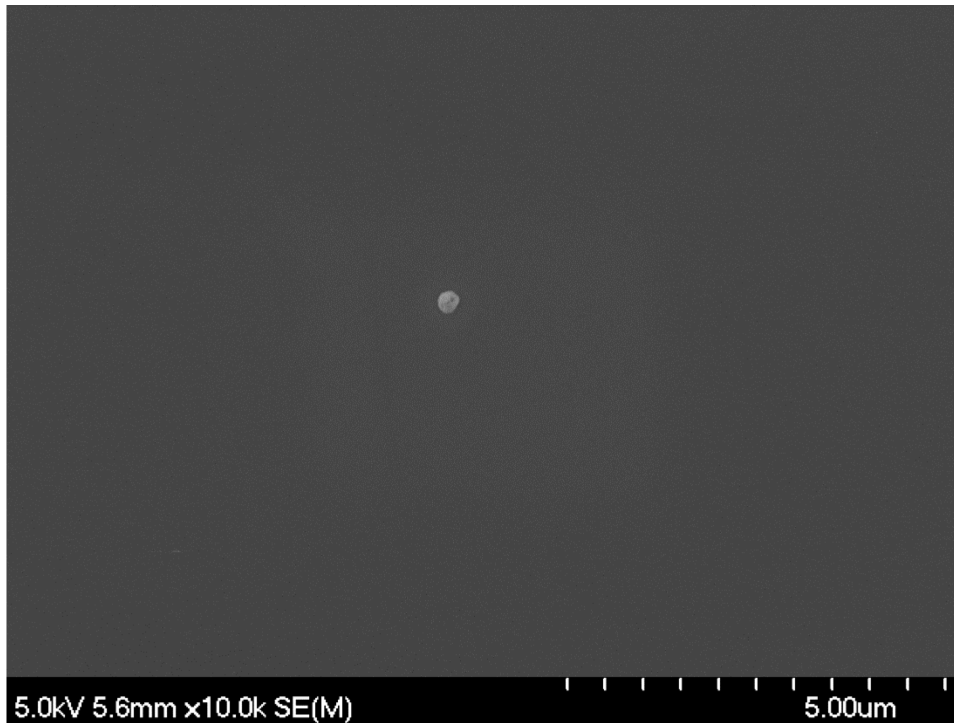


*Figure 22: S59_AH, SEM showing the only feature found that was reminiscent of the previously encountered blisters. This lead to the initial conclusion that blister formation had been successfully avoided via the move to lower $H_2$ partial pressures (in this case 0.3 mTorr $H_2$), and the inclusion of an RF plasma discharge. Density of this film was modelled to be 1.73 g/cm$^3$.*

AFM of this sample eventually indicated that blisters were present, though smaller in number and size as compared to previously detected bubbles. This indicated that the measures taken to avoid bubble formation were sound and, while not entirely sufficient with this sample, were certainly effective. By extension then, one can assume that even should the previously theorized process for bubble formation be only part of the complete process, it is generally correct.

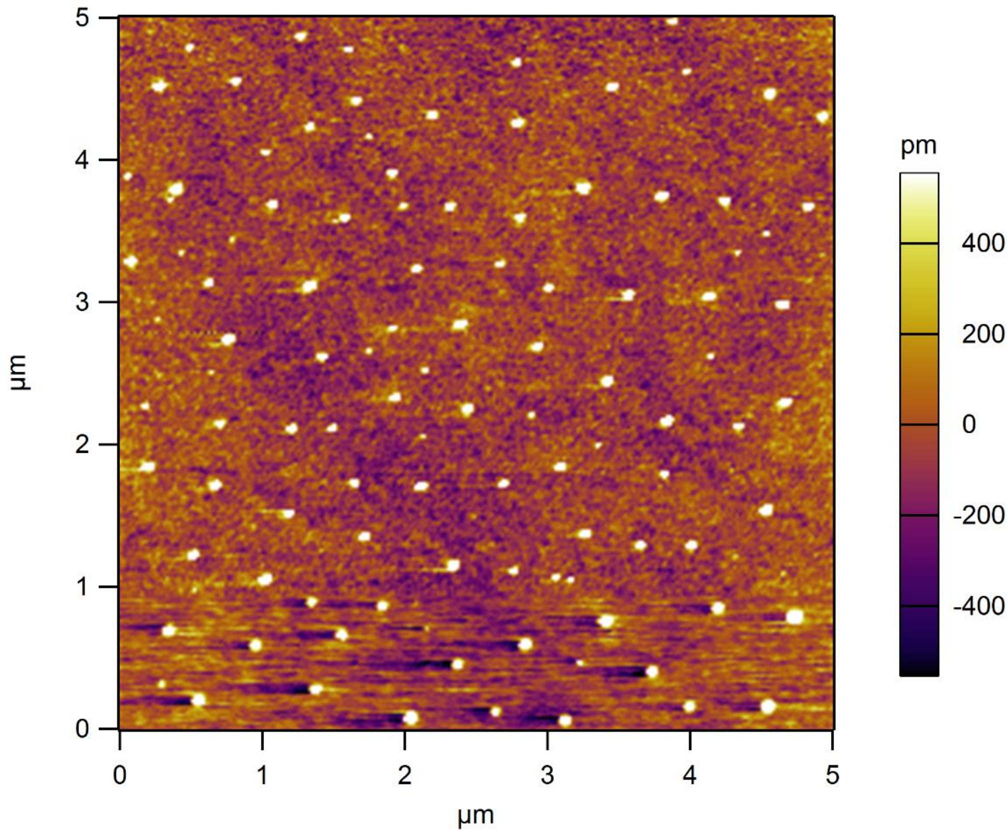


*Figure 23: AFM micrograph of S59_AH. Dashed hope provided by SEM scan of the same sample that blister formation had been dealt with, and yet also shows that the number of blisters, as well as their size, is significantly reduced.*

Due to heating concerns with respect to the RF plasma, modifications were made at this point to permit water cooling of the RF coil. Once these had been made, further tests were run, further attempting to eliminate the bubble growth issue. This primarily focused on modifying the deposition current setpoint, while maintaining the 0.3 mtorr $H_2$ partial pressure and 300W RF power plasma. Some trials were reasonably successful, some less so, with the caveat that even the more successful films, such as S68_AH, which was deposited at a $H_2$ partial pressure of 0.3 mtorr, 300W RF power, and 150mA of deposition current and was determined through modelling to have a density of 1.7 g/cm$^3$, had XRR spectra that could not be entirely explained. As such some of the more promising results among these, while worth mentioning, are still somewhat dubious. One interesting sample that was deposited during this time is S68_AH, which was deposited at 0.3

mtorr $H_2$, 300W RF, and 200mA deposition current. From previous data one would expect a reasonably good hydrogen incorporation in this sample. Instead, it is almost unique in showing a Si density of 2.3 g/cm$^3$, a value close to the tabulated Si density than the regular Si films that had previously been deposited. A comparatively high deposition rate of 12.6 nm/min additionally makes this type of setpoint less than ideal for the deposition of the ~4nm thick layer that would be necessary for a multilayer, and thus this setpoint was not explored much further.

### 4.3.1 Radical Probe Results

Characterization of the mixed hydrogen-argon RF plasma was carried out using catalytically-coated thermocouple radical probes. The experiment conducted was concerned with looking at the effect on the H radical density with respect to changes in $H_2$ partial pressure and RF power. These experiments were conducted towards the end of experiments and, therefore, the range of pressures and powers investigated were dictated by previous results. The hydrogen partial pressures investigated were 0.1, 0.2, and 0.3 mTorr, all in the presence of the ubiquitous 1.5 mTorr Ar. RF Power setpoints investigated were 100, 200, and 300 W net RF power. The results of this, comparatively, cursory testing is summarized below.

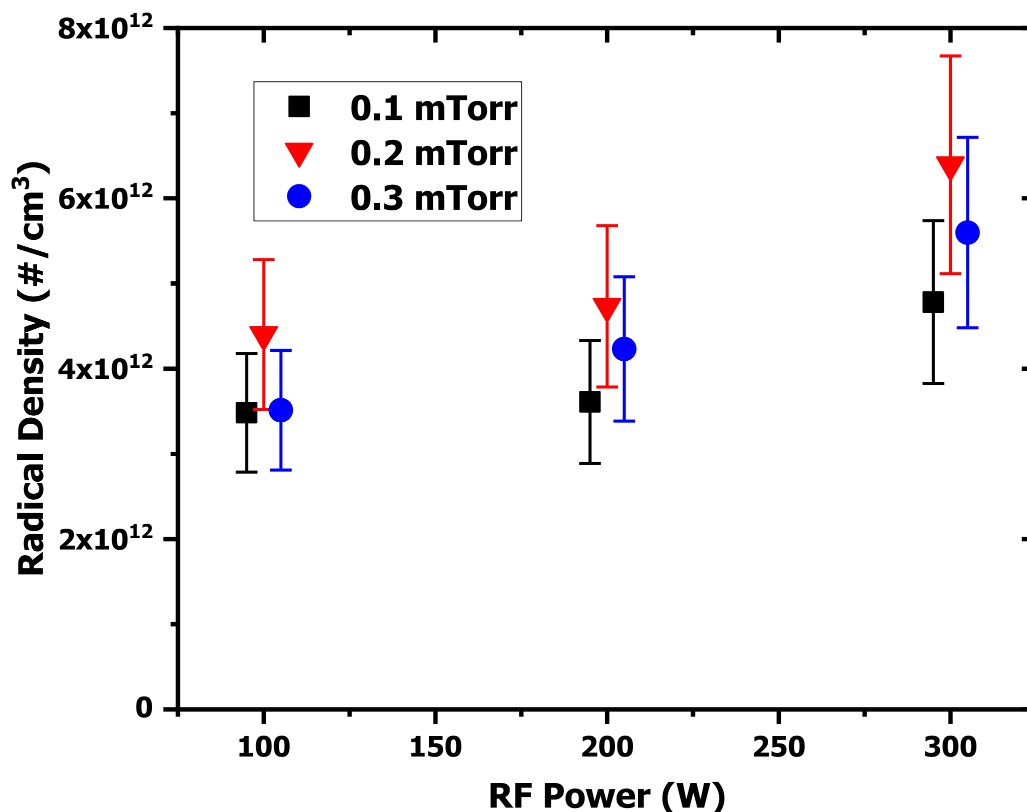


*Figure 24: Radical Probe data for first set of scans across 0.1, 0.2, and 0.3 mTorr $H_2$ and 100, 200, and 300 W RF Power. Note that while data points were consistently offset off the actual power value to permit for clearer understanding. Each cluster of data points corresponds to 100, 200, or 300 W RF. The general behavior of increased RF power increasing radical density conforms to expectations, however the behavior with respect to $H_2$ partial pressures does not.*

The results are generally as expected: with a higher $H_2$ partial pressure or a higher RF power setpoint leading to higher radical densities. It is worth noting here that while the absolute values of the radical density may not be entirely accurate, all the values were obtained in the same fashion and using the exact same probe. Therefore, while the quantitative results should be viewed with some care, the qualitative results are likely to be accurate. The most unexpected result presented here then, is that, regardless of the RF power supplied, the radical concentration is largest for the 0.2 mTorr $H_2$ partial pressure, beating out the 0.3 mTorr partial pressure in every case. Along with this, at the 100W RF setpoint, the 0.1 and 0.3 mTorr partial pressure measured radical densities are nearly identical. The reason for the behavior seen is unknown.

Due to this unexpected behavior of the radical density this same experiment was repeated, leading to the data seen below. As can be seen, this data completely opposes what is expected, with the radical density decreasing with increased $H_2$ partial pressure. Various thoughts have been put forward as to the reason for this behavior, but in the end, no clear conclusion can be drawn from this data without further study, such as knowing the plasma characteristics, which were not tested for in this experiment. Clearly, then, in the future a repeat of these experiments in combination with a technique for determining the plasma characteristics is necessary.

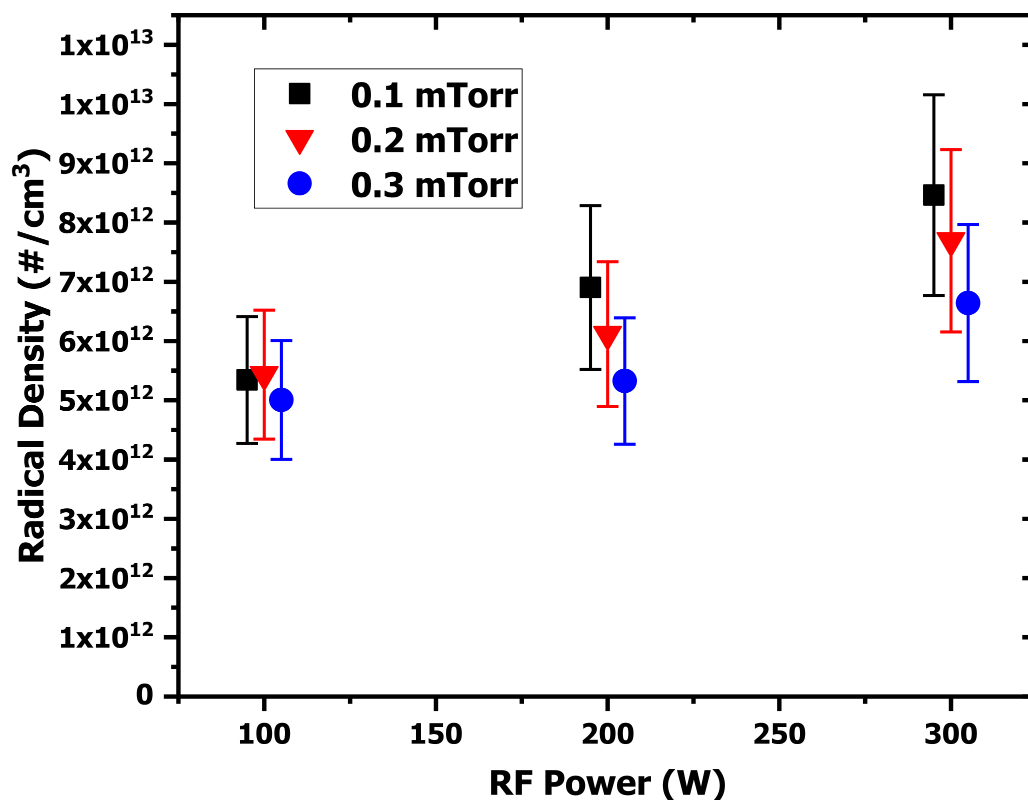


*Figure 25: Radical Probe data from second set of Radical probe scans. Same parameter field as before. Once again data points are offset w.r.t. RF power for clearer viewing. As previously, the behavior of radical density w.r.t. RF power confirms to expectation, and, once again, the behavior of radical density w.r.t. $H_2$ partial pressure does not match with expectation.*

## 4.4 Multilayer Films

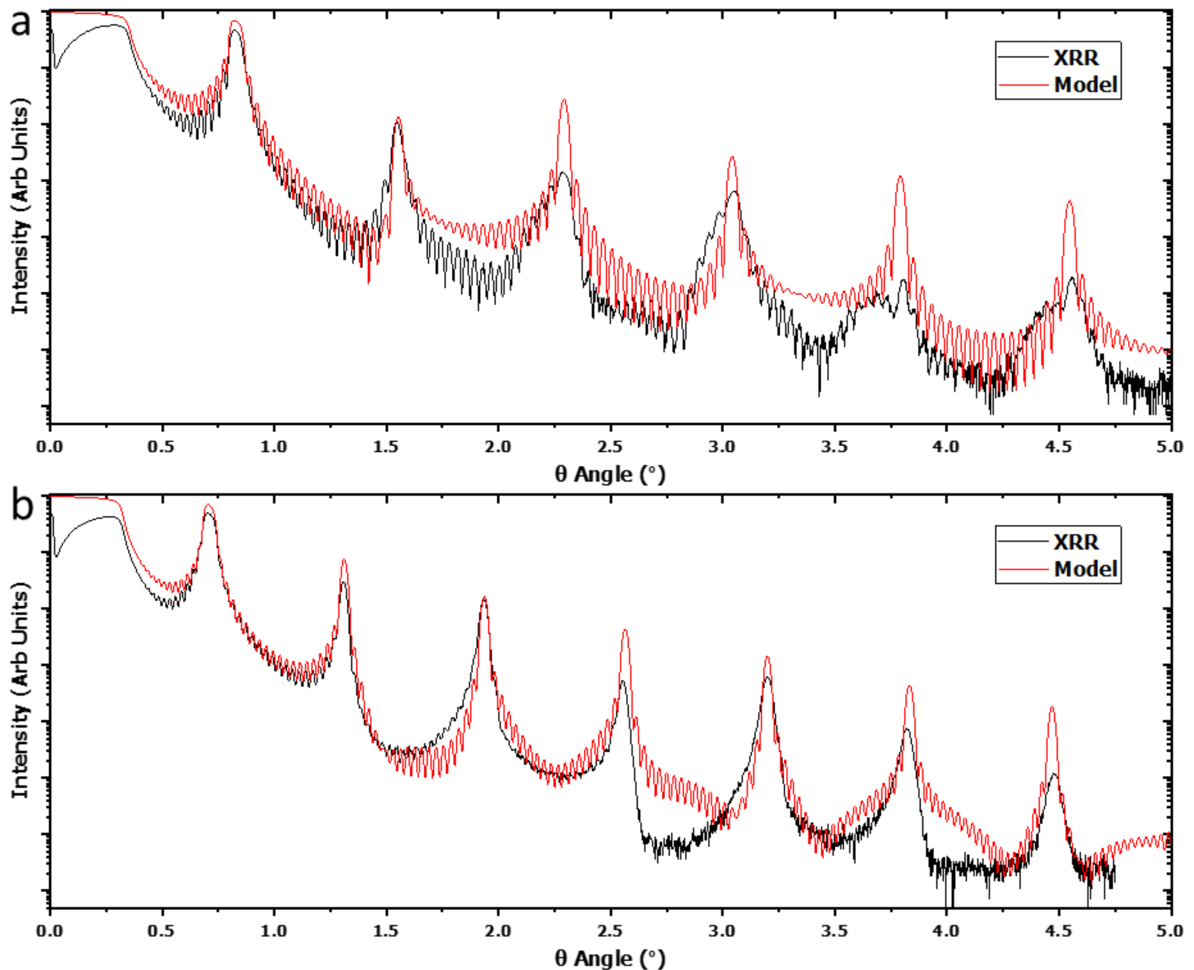


*Figure 26: Multilayer XRR scans and models. Demonstration of a) presence of shoulders on the main peaks and b) of their removal through thorough cleaning of target via extensive cleaning plasma. MLM represented in 'b' has Mo and Si thicknesses of 2.91 and 4.03 nm, respectively.*

Deposition of the multilayers was accomplished using the combination of both of the previously detailed deposition procedures for Mo and Si, with timing, and therefore thickness of the individual layers, controlled by a homebuilt LabView program which, in combination with a LabJack and a pneumatic switching valve, actuates a Kurt J Lesker pneumatic activated 2 position shutter, with the two positions calibrated to cover one or the other magnetron. A worthwhile note here is that it is generally recommended to utilize two distinct shutters, one for each magnetron,

but this was not implemented here due to space constraints. Mirroring previously stated procedures, deposition was performed on square, 2.5 cm a side single-crystal Si wafers. Setpoints that had been established during the deposition of the individual layers of Mo and Si were used for the deposition of the multilayer, along with a gas pressure of 1.5 mTorr Ar. The Bertan Series 105 Power supply was used throughout for the Si deposition, whereas, once again mirroring previously established behaviors, the Mo deposition was originally powered by an Advanced Energy Power supply, and later by a Magna Power Supply after the AE Power Supply died. The Mo setpoint changed accordingly. Deposition times were varied to achieve the eventual goal of d=7nm and Γ=0.43, leading to a Si layer thickness of 4nm and a Mo layer thickness of 3nm. As per usual, XRR was used for analysis of the multilayers, in which an unusual feature was observed in some multilayers. Namely, significant signal strengths of the minor peaks, rivaling the main peaks in intensity. This was thought to indicate a non-periodicity in the structure of the multilayer. The source of such non-periodicity is simple to imagine: changes in the deposition conditions during the actual deposition. As each multilayer took approximately 40 minutes, it is not hard to imagine that changes can occur in the plasma. The course of action taken was a simple one: instituting a more thorough cleaning plasma on the magnetrons before each individual deposition to ensure a properly "clean" target at the beginning of the deposition. While cleaning plasmas had always been performed intermittently before, now the goal was to run a thorough cleaning plasma until no significant change in the voltage was observable while the standard setpoint was applied. What was found in this way, was that the Si target required an approximately 40 min long cleaning plasma, until the voltage was entirely steady. This is, of course, the same time scale as that used in the actual deposition, certainly indicating that the deposition parameters were in fact changing

during the deposition due to self-cleaning of the target. With this modification made, the "shoulders" previously observed in the XRR profiles vanished.

# 5. Conclusion

The initial goal of this work was to produce a classical Si/Mo multilayer with the Si layer replaced by a reduced density, hydrogenated Si layer, in addition to a regular Si/Mo multilayer. Deposition of both of these films within the same deposition system and deposited to the same standards, that is bilayer thickness, d, layer thickness ratio, Γ, and number of periods, N, would permit easy comparison in a EUV reflectivity test to validate the concept. While this was not achieved in the end, significant progress towards it was made, namely reasonable quality 20 period multilayers were produced and it was shown that modification of the recipe for a specific structure is feasible in the available system.

The main component holding up the deposition of an Si:H/Mo multilayer then is the issue of the Si:H film. While reduced densities were clearly shown, managing to reduce the density down to 1.7 $g/cm^3$, the problem of $H_2$ blister formation during the deposition was observed. While measures to prevent blister formation were taken, and certainly progress in reducing the size and number of blisters observed was achieved, a full removal has not yet been accomplished.

# 6. Future Work

The possibilities for future work are, initially, clear cut: the production of a hydrogenated Si layer with reduced density, while also avoiding completely the formation of blisters in the film. To this end continuation of the approach taken so far, that is reduction in the $H_2$ partial pressure as well as an increase in RF power, may yield favorable results. The caveat here is that the $H_2$ partial pressure cannot be, practically, reduced much further in the current system with current equipment, both due to limits in the ability to control such low flow rates, as well as the ability to measure pressures accurately in the necessary range. Additionally, the move to higher RF powers may require cooling of the substrate, due to heating concerns in such close proximity to a RF plasma. A different approach that may be taken in these cases is a reduction in the deposition rate, which in turn will permit better regeneration of H radicals for the deposited material to react with. It may also be worth exploring other methods of deposition than DCMS, as the choice of DCMS was made primarily due to the current application of DCMS for the production of the regular Si spacing layer in commercial mirrors. Options can range from RFMS or HiPIMS to methods such as PECVD, though this is, in turn, less optimal specifically because it would require a major change in the method of production of commercial mirrors.

Once the challenges faced in creating a reduced density hydrogenated Si layer are met, the next logical step is to then incorporate such a layer in a multilayer with standard d and Γ, and compare the experimental EUV reflectivity between this reduced density Si multilayer with that of an equivalent normal Si multilayer produced in the same device. By controlling for all factors other than the reduction in density it should then be comparatively simple to measure the EUV reflectivity, and thereby finally clearly, and in practice, demonstrate that there exists a benefit to using a reduced density Si spacing layer in a multilayer mirror.

Once these tasks have been successfully accomplished, it may well be worth looking into the material possibilities for similar modifications to the spacing layers in non-EUV soft X-ray mirrors, though this is likely to deviate significantly from this project due to the changes in materials that become necessary. That said, if the possibility exist to create a reduced density spacing layers via the additional incorporation of hydrogen (or even other gases, the focus on hydrogen is simply due to the specific challenges faced with hydrogen,) then the lessons learned here may well be applicable in those other scenarios.

# 7. References

[1] G. Moore, "Cramming more components on integrated circuits," *Electronics,* vol. 38, 1965.

[2] W. A. Soer, P. Gawlitza, M. M. J. W. v. Herpen, M. J. J. Jak, S. Brain, P. Muys and a. V. Y. Banine, "Extreme ultraviolet multilayer mirror with near-zero IR reflectance," *Optics Letters,* vol. 34, no. 23, 2009.

[3] I. V. Kozhevnikov and A. Vinogradov, "Multilayer X-Ray Mirrors," *Journal of Russian Laser Research,* vol. 16, no. 4, pp. 343-385, 1995.

[4] A. G. Revesz, "On the Structure of Noncrystalline Si and Si1-xHx Films," *physica status solidi,* vol. 60, no. 2, 1980.

[5] V. G. Kohn, "On the Theory of Reflectivity by an X-Ray Multilayer Mirror," *physica status solidi,* vol. 187, no. 61, pp. 61-70, 1995.

[6] E. Gullikson, "X-Ray Interactions With Matter," [Online]. Available: http://henke.lbl.gov/optical_constants/.

[7] B. L. Henke, E. M. Gullikson and a. J. C. Davis, "X-Ray Interactions: Photoabsorption, Scattering, Transmission, and Refection at E = 50-30,000 eV, Z = 1-92," *Atomic Data and Nuclear Data Tables,* vol. 54, pp. 181-342, 1993.

[8] A. S. Kuznetsov, M. A. Gleeson and F. Bijkerk, "Temperature dependencies of hydrogen-induced blisering of thin film multilayers," *Journal of Applied Physics,* vol. 115, no. 17, 2014.

[9] D. T. Elg, J. R. Sporre, G. A. Panici, S. N. Srivistava and D. N. Ruzic, "In situ collector cleaning and extreme ultraviolet reflectivity restoration by hydrogen plasma for extreme ultraviolet sources," *Journal of Vacuum Science & Technology,* vol. 34, no. 2, 2016.

[10] T. Tanabe, Y. Tamanishi and a. S. Imoto, "Hydrogen permeation and diffusion in molybdenum," *Journal of Nuclear Materials,* Vols. 191-194, pp. 439-443, 1992.

[11] R. Raju, L. Meng, R. Flauta, H. Shin, M. Neumann, T. Dockstader and D. Ruzic, "Development and characterization of a secondary RF plasma-assisted closed-field dual magnetron sputtering system for optical coatings on large-area substrates.," *Plasma Sources Science and Technology,* vol. 19, no. 2, 2010.

[12] M. Alam, R. Pulavarthy, J. Bielefeld, S. King and M. Haque, "Thermal Conductivity Measurements in Low-k Dielectric Films: Effects of Porosity and Density," *Journal of Electronic Materials,* vol. 43, no. 3, 2014.

[13] F. Sarubbi, L. Nanver, T. Scholtes, S. Nihtianov and F. Scholze, "Pure boron-doped photodiodes: A solution for radiation detection in EUV lithography," *ESSDERC 2008 - 38th European Solid-State Device Research Conference,* pp. 278-281, 2008.

[14] I. Makhotkin, E. Zoethout, E. Louis, A. Yakunin, S. Müllender and a. F. Bijkerk, "Spectral Properties of La/B - based multilayer mirrors near the boron K absorption edge," *Opt. Express,* vol. 20, no. 11, pp. 11778-11786, 2012.

[15] M. A. Lieberman and a. A. J. Lichtenberg, Principles of Plasma Discharges and Materials Processing, Hoboken, New Jersey: John Wiley & Sons, Inc.,, 2005.

[16] D. B. Hayden, "Helicon plasma source for ionized physical vapor deposition," *Surface and Coatings Technology,* Vols. 120-121, pp. 401-404, 1999.

[17] J. Hopwood, "Review of inductively coupled plasmas for plasma processing," *Plasma Sources Sci. Technol.,* vol. 1, no. 109, 1992.

[18] L. Meng, *Plasma Diagnostics and ITO film deposition by RF-assisted Closed-Fidl Dual Magnetrons System,* 2010.

[19] D. E. Barlaz, "New Strategies For Application Of Defect Engineering To TiO2 Based Photocatalytic Materials," 2017.

[20] M. Mozetic, M. Drobnic, A. Pregelj and a. K. Zupan, "Determination of density of hydrogen atoms int eh ground state," *Vacuum,* vol. 47, pp. 943-945, 1996.

[21] F. Brecelj, M. Mozetic, K. Zupan and M. Drobnic, "Behavior of Catalytic probes at low pressure," *Vacuum,* vol. 44, pp. 459-460, 1993.

[22] M. Mozetic, A. Vesel, A. Drenik, I. Poberaj and D. Babic, "Catalytic probes for measuring H distribution in remote parts of hydrogen plasma reactors," *Journal of Nuclear Materials,* 2007.

[23] D. T. Elg, G. A. Panici, J. A. Peck, S. N. Srivastava and a. D. N. Ruzic, "Modeling and measurement of hydrogen radical densities of in situ plasma-based Sn cleaning source," *Journal of Micro/Nanolithography, MEMS, and MOEMS,* vol. 16, no. 2, 2017.

[24] M. J. H. Kessels, J. Verhoeven, F. D. Tichelaar and F. Bijkerk, "Si adhesion interlayer effects in hydrogen passivated Si/W soft X-ray multilayer mirrors," *Surface Science,* vol. 600, pp. 1405-1408, 2006.

[25] Argonne National Laboratory, "Software Download for XOP v2.4 and Future Releases," [Online]. Available: https://beam.aps.anl.gov/apps/xop/. [Accessed 7th July 2019].

[26] D. L. Windt, "IMD -- Software for modeling the optical properties of multilayer films," *Computers in Physics,* vol. 12, no. 4, pp. 360-370, 1998.